POLITECNICO DI TORINO

Master degree course in Mechanical Engineering

Master Degree Thesis

A Full Field Calibration Approach on Material Parameter identification

Supervisors

prof. Alessandro Scattina

Candidates

Simone Cavariani

matricola: 234882

Internship Tutor

dott. ing. Salvatore Scalera

APRILE 2019

To my family

Acknowledgements

I kindly thank for their constant support my supervisors and my colleague at DYNAmore Riccardo. My friends and my family that have stuck with me all this time, enduring my craziness and engineering student career.

Abstract

Steel components are omnipresent of the automotive field. Their wide variety of characteristics, they go from being very hard and brittle to extremely ductile, can fulfill many automotive designers needs. Their precise and accurate study can increase safety, fuel efficiency and overall product profitability. In this context, for the design with any material it has become crucial to be able to characterize precisely steels and accurately predict their failure in many complex conditions.

One of the most accredited ways to approach the prediction of failure for a wide range of materials is the generalized incremental stress-state dependent damage model GISSMO. The model is highly flexible and provides a framework inside LS-DYNA in which failure parameters can be tuned to reproduce experimental data. The definition of the optimal parameters is an inverse problem, therefore it was implemented using LS-OPT.

In this work, the experimental evaluation of a MS1500 and a DP800 was carried out using the digital image correlation (DIC). With such technology, the displacement field of the test specimen is recorded.The evalueted field was processed as a family of stress-strain curves (hyper-curves) and became the objective of the optimization. This approach is named full field calibration and the aim of this work is to evaluate the effectiveness of the introduction of

field data in the characterization of steels. This work was split in two phases. First, the stress-strain curve of the material was defined, then the tuning of the GISSMO parameters was performed.

To evaluate the effectiveness of the full field approach a parallel study was implemented. The same routine of optimization run with a single stress-strain curve, which was measured with an extensometer. The comparison between the results obtained with the traditional approach and the results obtained with the full field approach highlighted the strenghts and the limitations of the two methods.

Contents

List of Tables

List of Figures

12

Chapter 1

Introduction

Nowadays the possibility to accurately simulate the materials is crucial to expect accurate results in finite element analysis. Just as much as boundary conditions, joints and fixtures, more precise material models are continually sought after throughout the industry. Material calibration for is important in applications with large deformations and fully plastic cases like forming and crash simulations where simple linear models fail to achieve the desired accuracy.

More complex model require a significant effort to calibrate them to the physical behavior of the materials, but can perform better. This work will evaluate and compare different techniques to characterize materials for finite element simulations.

1.1 Objectives

The objective of this thesis work is to analyze the effectiveness of a new material calibration technique called "Full field calibration". The typical operation

in a steel testing application would employ a universal testing machine together with an extensometer to measure the tensile load and displacements during the test. The displacements measured are then used to compute the average strain between the measuring points. Due to the advent of new strain measurement technologies, such as digital image correlation, it is now possible to acquire and analyze the strain field, from the local displacement on the surface. The possibility to include in the material model information coming from the whole analyzed piece, or at least a significant region of it, allows for the richer description of its behaviour. This technique also permits to inspect the necking area, which is affected by the highest strains and strain gradient.

Two materials will be tested, a martensitic high strength steel (MS1500) and a more ductile dual phase steel often utilized in automotive application (DP800). The characterization will be split in two parts: the determination of the yield curve of the materials and the optimization of a failure model. For the first part three approaches are tested. The new approach, "Full field Calibration" (FFC), which includes strain field data in the optimization of the yield curve. Then, the "Standard" way, which only uses the displacement data of an extensometer, and lastly the "Volume Conservation (VC)" method, which is explained in detail in section (5.3). For the second part, the failure model optimization will be carried out in just the FFC and Standard ways.

1.2   Overview of the Thesis

The Master's Thesis work is organized as follows. Chapter (2) illustrates the background knowledge necessary to confidently approach the analysis

performed in this work. Chapter (3) describes the experimental study that was performed to collect experimental data for the subsequent calculations. Chapter (4) presents the considerations that guided the preparation of the finite element models that were used in the optimizations. Chapter (5) reports about the preparation of the yield curve optimization and discusses the obtained results. Chapter (6) follows Chapter (5) structure, but describes the optimization of the failure model and the results that it produced. The last Chapter, (7), summarizes the results of this work and presents the possible future developments.

Chapter 2

Theoretical Background

This chapter aims to present all the relevant theoretical knowledge needed to approach this work. Section (2.1) presents the tools necessary to describe the state of a deformed metal. Section (2.2) aims to outline the study of the plastic deformation in metals and the mechanics that lead to their failure. Sections (2.3) and (2.4) include an overview on the experimental techniques used to study the mechanical properties of the alloy provided by FCA and on the optimization technique theories required to calibrate the parameters used to simulate the material behavior.

2.1   Stress and strains in metals

A theory which tries to describe the mechanical behavior of a material focuses on searching for the relationship between the strains and stresses inside said material. This means investigating how the material deforms when subjected to forces, and linking the strains and stresses from the displacements to the applied forces. These relationships can be quite simple for mono-dimensional

geometries and small loads. They become more complicated when describing the 3-D world and phenomena like yielding and plasticity occurs.

At the base of the investigation on the deformation of metal is the uni-axial tensile test. A simple straight specimen is subjected to a quasi-static increasing load along one direction until failure occur. Due to the simple nature of the test it si possible to define *nominal stress*

$$\hat{\sigma} = \frac{F}{A_0} \tag{2.1}$$

and *nominal strain*

$$\hat{\epsilon} = \frac{l - l_0}{l_0} \tag{2.2}$$

in which F represents the load, A_0 represents the nominal cross-section and l_0 represents the initial length of the test specimen. These entities are defined on the initial state of the testing sample. It is apparent from experimental data that the cross-section does not remain constant during the test. On the other hand, it is possible to introduce *true* or *Cauchy stress*

$$\sigma = \frac{F}{A} \tag{2.3}$$

and *true* or *logarithmic strain*

$$\epsilon = \frac{dl}{l} \text{ or } \epsilon = \int_{l_0}^{l} \frac{dl}{l} = ln\frac{l}{l_0} \tag{2.4}$$

which are defined on the instantaneous cross-section and length. By looking at equation (2.2) and (2.4) it is easy to obtain

$$\epsilon = ln(1 + \hat{\epsilon}) \tag{2.5}$$

which describes the relationship between the two strains, and this holds in any case. On the other hand, a similar relationship with stresses is based on the assumption of volume conservation and homogeneous stress state, which are true until the point of uniform elongation [1].

$$A_0 \cdot l_0 = A \cdot l \tag{2.6}$$

therefore

$$\sigma = \frac{F}{A} = \frac{F}{A_0} \cdot \frac{l}{l_0} = \hat{\sigma}(1 + \hat{\epsilon}) \tag{2.7}$$

Equations (2.5) and (2.7) can be used to transform one kind of stress or strain to the other.

2.1.1   Von Mises stress

The previous section dealt with a simple mono-dimensional case. When dealing with complex geometries, loading conditions and constraints, the stress state is represented by the Cauchy stress tensor with its nine components in a (x, y, z) coordinate system:

$$\boldsymbol{\sigma} = \begin{bmatrix} \sigma_{xx} & \sigma_{xy} & \sigma_{xz} \\ \sigma_{yx} & \sigma_{yy} & \sigma_{yz} \\ \sigma_{zx} & \sigma_{zy} & \sigma_{zz} \end{bmatrix} = \begin{bmatrix} \sigma_{xx} & \tau_{xy} & \tau_{xz} \\ \tau_{yx} & \sigma_{yy} & \tau_{yz} \\ \tau_{zx} & \tau_{zy} & \sigma_{zz} \end{bmatrix} \tag{2.8}$$

It is uniquely determined by six independent values. The matrix must be symmetric to satisfy the rotational equilibrium. For clarity a graphical representation is shown in figure (2.1).
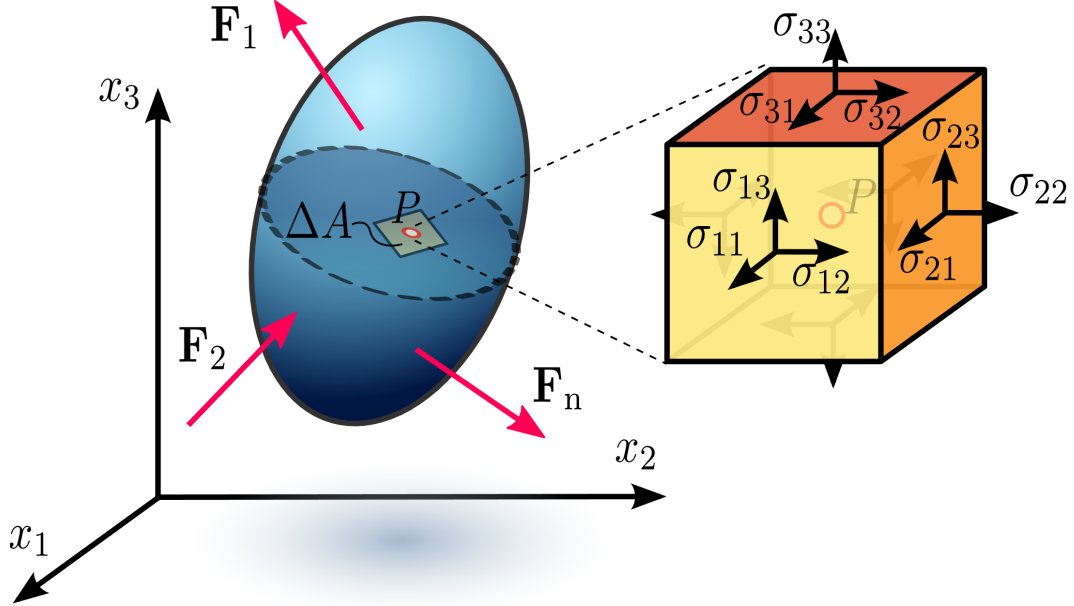
Figure 2.1: Components of a stress tensor inside a body [2]

The need to compare quantitatively different stress states drove the development of effective criteria. Huber [3] and Von Mises [4] later proposed the calculation of an equivalent stress that could condense most the information carried by the Cauchy stress tensor. They started by dividing the stress tensor into two parts, hydrostatic and deviatoric. Given the ij components of the stress tensor it is possible to write:

$$\sigma_{ij} = p \cdot \delta_{ij} + S_{ij} \tag{2.9}$$

where p is the hydrostatic stress, S is the deviatoric stress tensor and δ_{ij} is the Kronecker delta. p and S are calculated, respectively:

$$p = \frac{1}{3}\sigma_{ij} = \frac{1}{3}(\sigma_{xx} + \sigma_{yy} + \sigma_{zz}) \qquad (2.10)$$

$$S_{ij} = \sigma ij - p \cdot \delta_{ij} \qquad (2.11)$$

It is now possible to write the second invariant J_2, the deviatoric stress tensor:

$$J_2 = \frac{1}{6}\Big[(\sigma_{xx} - \sigma_{yy})^2 + (\sigma_{yy} - \sigma_{zz})^2 + (\sigma_{zz} - \sigma_{xx})^2\Big] + \sigma_{xy}^2 + \sigma_{yz}^2 + \sigma_{xz}^2 \quad (2.12)$$

Huber and Von Mises' assumption was that yielding occurs when the second invariant J_2 of the deviatoric stress tensor S reaches a critical value k^2. To determine the value of k[5] it is possible to use a simple uniaxial tensile test, in which the stress at the yielding point is measured. Using a principal
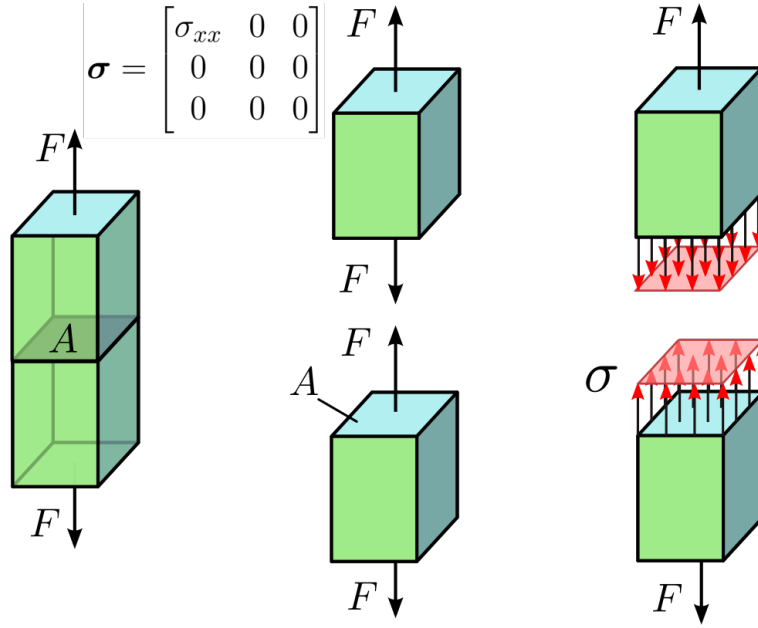
Figure 2.2: Ideal representation of the uniaxial tensile test [6]

reference system, with the x axis parallel to the direction of application of the load as shown in figure (2.2), the Cauchy stress tensor is reduced to one scalar:

$$\sigma_{xx} = \sigma_y \text{ and } \sigma_{yy} = \sigma_{zz} = \sigma_{xy} = \sigma_{xz} = \sigma_{yz} = 0 \qquad (2.13)$$

and J_2 becomes:

$$\frac{1}{3}\sigma_y^2 = k^2 \text{ so that } k = \frac{\sigma_y}{\sqrt{3}} \qquad (2.14)$$

Using the results of the experiment, the Von Mises criteria can be expressed as a simple inequality including the equivalent Von Mises stress σ_{vm}:

$$\sigma_{vm} > \sigma_y \qquad (2.15)$$

In which σ_{vm} can be calculated as follows:

$$\sigma_{\mathrm{vm}} = \sqrt{\sigma_{xx}^2 + \sigma_{yy}^2 + \sigma_{zz}^2 - \sigma_{xx}\sigma_{yy} - \sigma_{yy}\sigma_{zz} - \sigma_{zz}\sigma_{xx} + 3\left(\tau_{xy}^2 + \tau_{yz}^2 + \tau_{zx}^2\right)} \qquad (2.16)$$

Equation (2.15) makes it possible to assess if the stress state, represented in all its components, is such that yielding occurs.

$$\sigma_{vm} > \sigma_y \qquad \text{yield} \qquad (2.17)$$

$$\sigma_{vm} < \sigma_y \quad \text{no yield} \qquad (2.18)$$

2.2 Material plasticity

Von Mises yield criteria is one of the possible ways to identify the surface in the stress state space that separates elastic from plastic deformation. Equation (2.16) can be rewritten in a generic reference frame, equation (2.19), or in a principal reference frame, (2.20).

$$\sigma_{vm} = \sqrt{\frac{1}{2}\left[(\sigma_{xx} - \sigma_{yy})^2 + (\sigma_{yy} - \sigma_{zz})^2 + (\sigma_{zz} - \sigma_{xx})^2\right] + 3\left(\tau_{xy}^2 + \tau_{yz}^2 + \tau_{zx}^2\right)}$$

$$(2.19)$$

$$\sigma_{vm} = \sqrt{\frac{1}{2}\left[(\sigma_1 - \sigma_2)^2 + (\sigma_2 - \sigma_3)^2 + (\sigma_3 - \sigma_1)^2\right]} \qquad (2.20)$$

Equation (2.20) identifies a surface on the σ_1, σ_2 and σ_3 stress space, along which the value of σ_{vm} is constant. Elastic deformation occurs inside the surface and the deformation outside is plastic and non-reversible. A graphical representation of the Von Mises yield surface in a σ_1-σ_2-σ_3 space is presented in figure (2.3).
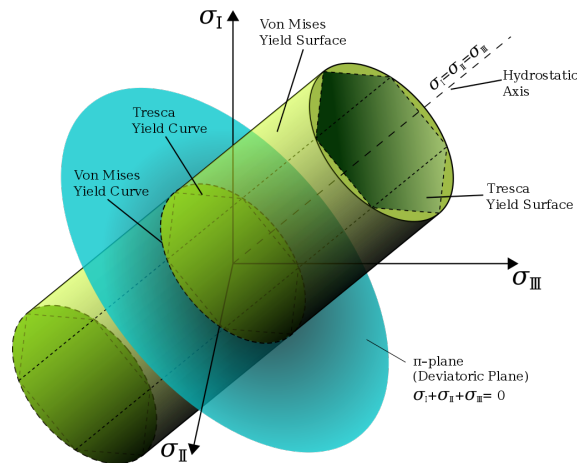
Figure 2.3: Von Mises Yield Surface [7]

The mechanical properties of a material heavily depend on its micro structure. Yielding depends on the crystal lattice that constitutes metals. The fundamental mechanic that allows the plastic deformation is the movement of atoms inside the lattice along slip planes. Dislocations are defects in the metallic lattice, and they move inside the lattice allowing it to deform in a non reversible way. Figure (2.4.a) shows how atoms are arranged inside a metal. One type of dislocation called edge dislocation describes a void, or missing atom, inside the crystal. These defects allow the breaking and reforming in different locations of the atomic bonds that hold the lattice together.
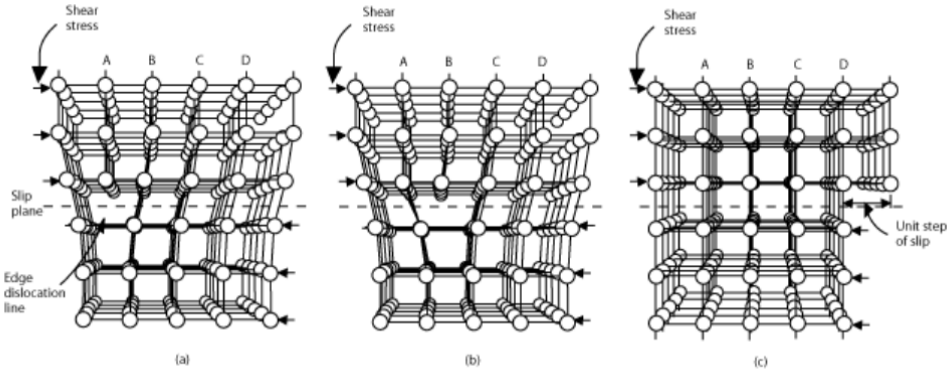
Figure 2.4: Cristalline structure of a metallic material with an edge dislocation [8]

When a shearing load is applied, as shown in figure (2.4.b), the lattice moves along the slip plane, highlighted with a dotted line in figure (2.4), and the bonds around the dislocation are modified, leaving a permanent deformation inside the material. The presence of a defect lowers the amount of force needed for the slip to occur because only a fraction of all the bonds needs to be broken concurrently.

Slip planes are randomly oriented inside the metal grains and this usually results in a mostly isotropic behavior of the metal. This behavior is lost gradually with plastic deformation as the slip planes tend to align along each other. Also during deformation the density of dislocations rises significantly, making subsequent deformation harder to achieve. The high number of dislocations generates fields of plastic deformation that hinder further movement. This phenomena is called work hardening.

Work hardening or strain hardening was estensively investigated by Hockett ans Sherby. To study materials after large deformation, when said phenomena occurs, they subjected a vast number of cylindrical specimen to uniaxial compression. The experiments led to the proposal of a relation that describes the true stress-strain curve [9]:

$$\sigma = \sigma_s - (\sigma_s - \sigma_y) \cdot e^{\left(-N\epsilon^P\right)} \tag{2.21}$$

2.2.1 Damage modelling

A model of damaged ductile material is necessary to accurately describe the failure and fracture of ductile materials, particularly in steels [10]. Modelling the plastic behaviour of metals can be done microscopically or macroscopically. Microscopic models take into account the crystal structure and the movement of dislocations. Macroscopic or phenomenological models reproduce the behavior of the material using experimentally tuned models.

The approach chosen in this work follows the macroscopic approach, more precisely the experience of Lemaitre [11]. It analyzes the phenomenon of micro-crack growth induced by large deformations in metals. This kind of

damage happens at a much bigger scale than the characteristic size of a metallic lattice. Lemaitre introduces a Damage variable D to quantify the presence of voids and micro-cracks in a given portion of material. Lemaitre interprets damage as a reduction of the effective area that can withstand stress. The damage variable corrects the effective area keeping into account only the portion that can still resist the load. D is defined as:

$$D = \frac{S - \overline{S}}{S} \tag{2.22}$$

S is the nominal area, $\overline{S}$ is the portion that is not damaged. D is the corrected area of cracks and voids per unit surface. Its values range from 0 to 1, where 0 represents the undamaged state and 1 represents rupture of the element. The surface in which the effective area is calculated is identified by the normal n and a representation is presented in figure (2.5).
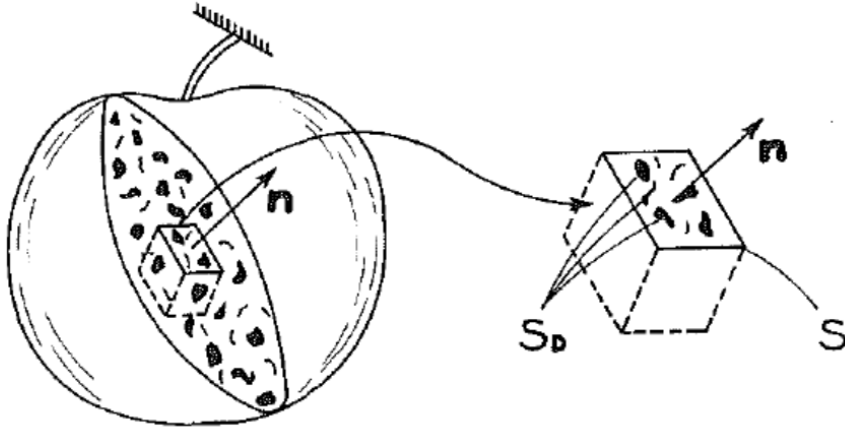

Figure 2.5: Voids generated by plastic strain in an element of metal and the relative effective area [11]

In most alloys, void nucleation begins at very low deformation values, and the progression of the damage and how fracture begins and grows is tightly

linked to how these voids grow and coalesce. The main parameter that influences the initiation of ductile damage, not taking into account stress intensity, has been shown to be stress triaxiality [10]. When dealing with complex geometries and loading conditions, such as those present in forming or crash analysis, the damage parameters that come from simple tensile tests are often unsatisfactory. This has suggested the need to use multiple geometries in test experiments, to test a range of values of triaxiality that ideally cover all the possible values that the piece could experience in its working conditions.

2.3 Material testing with digital image correlation

One of the technologies that made this work possible is digital image correlation (DIC) which is used extract displacements from material tests. Strain is traditionally measured using extensometers. This technique yielded one measurement series per specimen, along the instrument's gauge length. DIC is instead capable of a non intrusive full-field measurement of the displacements using one or more cameras to record the deformation of the test specimen.

For the DIC to be effective, the object being studied needs to present unique features that can be identified and followed during the experiment. Metals in their crude form are usually shiny and smooth, which makes them inadequate for optical correlation techniques. The state of the art technique for DIC involves applying a stochastic speckled pattern on the piece, or on the region of interest, with two passes of a white and black paint. Figure (2.6) presents one of the samples used in this work and highlights the applied pattern. This stochastic pattern doesn't have repeating features that could

lead to duplicated matching and optimally facilitates correlation software. Furthermore, the pattern is isotropic and presents high contrast between the image's white and black parts; this allows for unencumbered measuring sensitivity relating to the metal orientation or the direction of material flow.
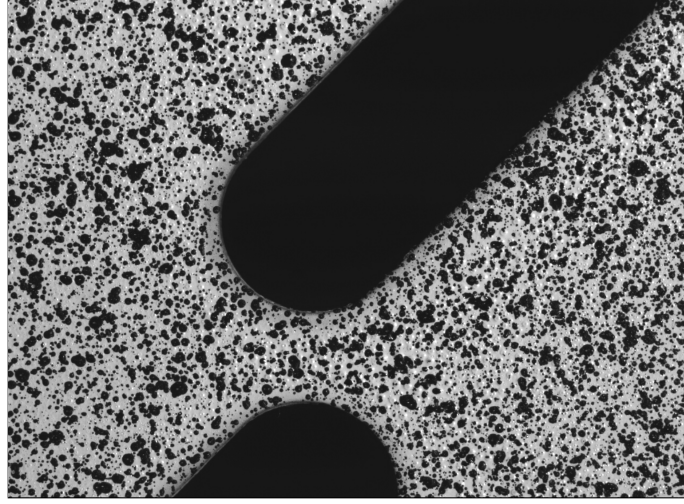
Figure 2.6: Particular of one of the shear test specimen with the DIC speckled pattern

The software uses pictures of the test specimen captured sequentially. First a reference picture is selected. Then a grid of measuring points is created on top of the speckled pattern. Every point in the mesh represents the center of a *facet*, which is a square collection of pixels. This is the fundamental object that the software will follow during the test. The strain field is obtained by combining the displacements and strains of all the facets. The facet size, which influences how many pixels it includes, and the distance between two adjacent facets can be chosen freely. To achieve a correct matching of the strains, facets should not be too small, or the correlation software will not have a sufficient number of unique features to find in the following

picture. Increasing the facet size benefits the matching, but it decreases the resolution at which the strains are calculated, possibly losing local peaks. The facet distance is set up to have a partial overlap between facets to avoid regions not covered by any facet.
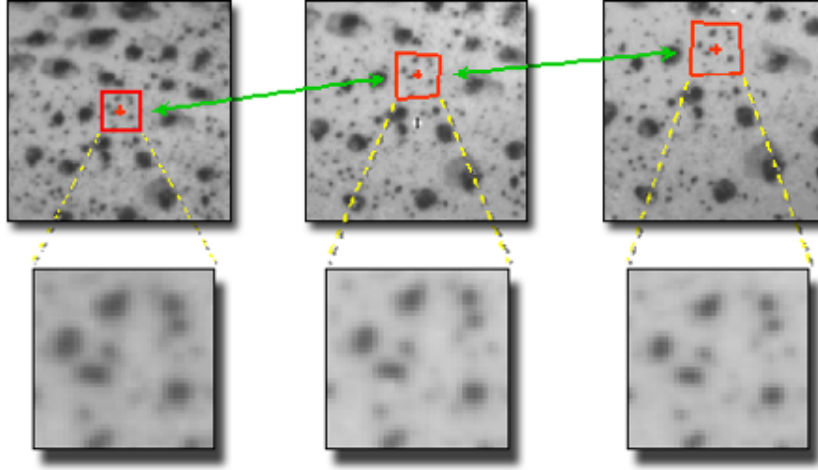
Figure 2.7: Facets of subsequent deformation located on the speckled pattern

Figure (2.7) displays how one facet is followed in three different time instants. Matching between pictures occurs in the software by comparing the distribution of whites, blacks and greys in a selected facet with candidates taken in the following pictures. The software utilizes a least square correlation function that provides a rate for the similarity of two facets. This process is repeated for all the facets and all the pictures and allows for visual representations and contours, like Figure (2.8). The field data extracted with DIC has been used to tune a material model to the experimental field of strain. Utilizing much more data, not only to a single average value but also to a distribution of values, allows for a better description of the material behaviour.

31
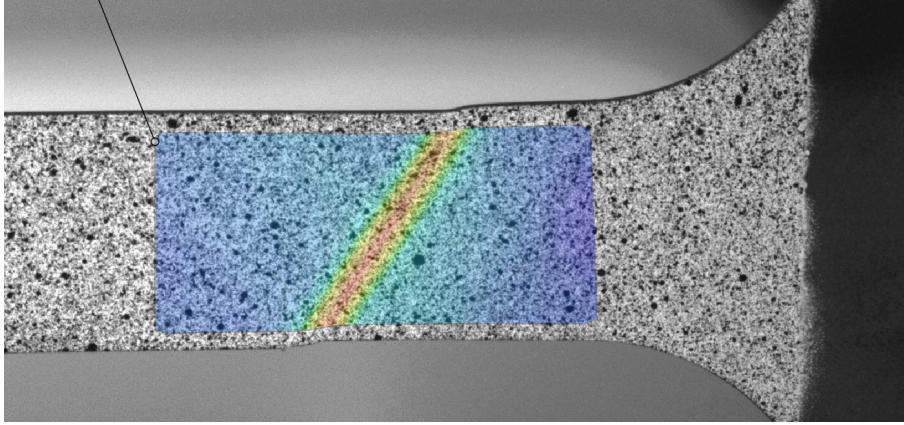
Figure 2.8: Contour plot of the major strain in a test specimen

2.4 Design Optimization

The conventional approach when faced with an engineering task is to study the problem and to propose a design that could be the solution. Then, the design has to be verified and changes may be added to satisfy safety criteria or to improve performance. These changes could be rational, intuitive or a mixture of both.

Nevertheless, design optimization takes a different approach. First, the problem is parametrized, and *design variables* are identified. These variables are restricted into a practical range, and the combination of all their possible values is called *design space*. Then, a group of rules and objectives to quantify the quality of the design is set. The next task involves exploring the design space to find the optimal design, in the most computationally efficient way. The quantification of the "goodness" of the design is done by evaluating each design's outputs, or *responses*, which can be displacements, stresses, frequencies or anything of significance for the specific task. The design's responses are compared against the corresponding desired outputs

to calculate the value of an *objective function*. The minimum of this function represents the optimal correspondence between the desired responses and actual responses. Constraints can be added to restrict certain responses, ruling out the designs that violatethem. The optimum design is discovered by searching for the minimum of the objective function.

Figure (2.9) and table (2.1) summarize a very simple illustrative optimization problem. A vehicle collision with a pole is simulated and the design of the bumper is the objective of the optimization.

Bumper study	
Responses	ϵ of the bumper
Objective	minimize intrusion
Constraints	max acceleration $< C$
Variables	bumper thickness
	bumper material
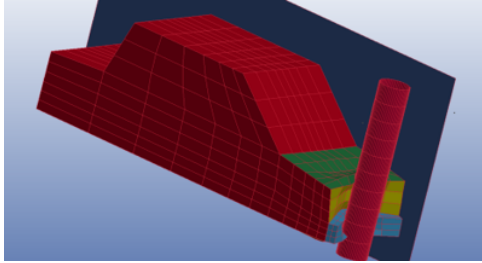
Figure 2.9: Crash simulation   Table 2.1: Significant parameters

It is searched for the optimal combination of material and thickness of the bumper that minimizes the intrusion of the pole and satisfies the safety constraint on the acceleration recorded inside the car body.

2.4.1   Optimization strategies

There are different optimization strategies to approach highly non linear optimization problems. The simplest way is gradient based methods, which require computing the objective function gradient in one of two ways. The first way involves analytical computation, which is usually too complicated

or impossible. The second way includes numerical estimation through perturbating the design, simulating a response from the system:

$$\frac{df(x,y)}{dx} \approx \frac{f(x + \triangle x, y) - f(x,y)}{\triangle x} = \frac{\triangle f}{\triangle x} \qquad (2.23)$$

This process is computationally expensive, for a system with n variables $n+1$ simulations are needed, and error prone. If the size of the perturbation $\triangle x$ is
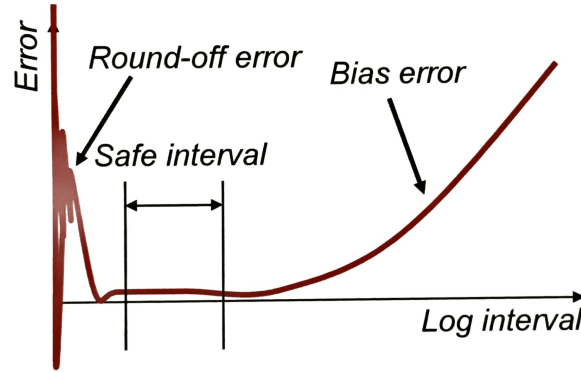
Figure 2.10: Error evolution as a function of $\triangle x$

too big there is a loss of accuracy of the calculated gradient. Round-off errors and a spurious dependency on the size arise if the perturbation is too small. This is due to noise and numerical errors. Figure (2.10) shows a qualitative representation of the error as a function of $\triangle x$.

Another possible way involves using Genetic algorithms. This name and the functioning principle is inspired from Darwin's theory of evolution. The algorithm starts with a population of individuals within the design space, and applies changes to each individual for a number of generations, ultimately selecting the fittest. The fitness is analogous to the previously mentioned objective function where the fittest has the lowest objective value. First the population is analyzed and the best individuals are selected. To proceed to

the next iteration operations of crossover and mutation are carried out and the new generation's population is formed. One of the advantages of this algorithm is that it is a global optimizer and where other methods could get stuck in local minima, the genetic algorithm finds the global one. Figure (2.11) is a block diagram of a simple genetic algorithm functioning scheme.
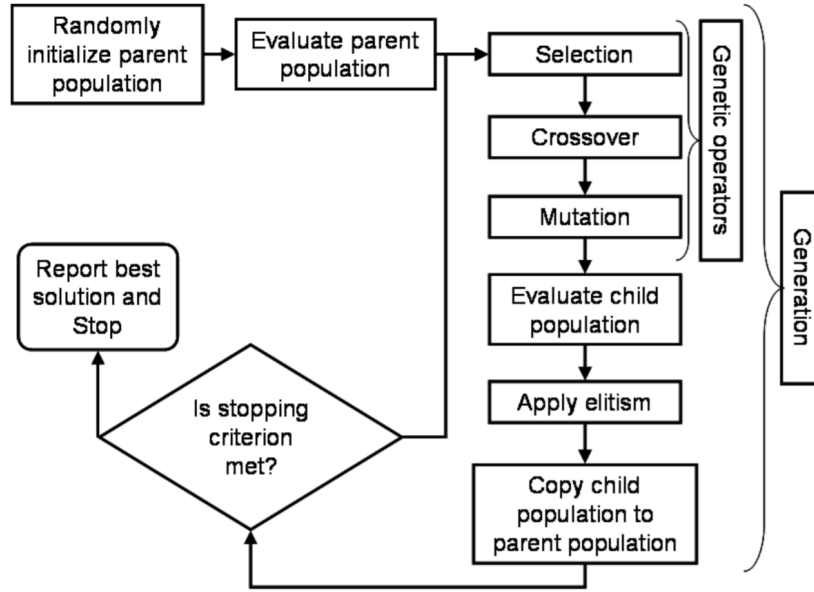
Figure 2.11: Simple Genetic Algorithm[12]: functioning scheme

A third technique used is the response surface methodology. This technique constructs an approximation of the design metamodel or response surface, and uses this simpler model to find the optimum values of the design variables. Figure (2.12) presents how this method would analyze a bi-dimensional problem. The procedure for finding the combination of x_1 and x_2 that minimize the objective involves sampling the design space for a number of points instead of evaluating every possible pair. The number and the location of the points depends on the metamodel formulation. The objective is then evaluated at these points and the values are used to create a response

surface. The candidate optimum is located on the response surface and it is verified if the system behaves as the approximated metamodel. If this is true the optimum has been found, otherwise the optimization continues iteratively, with more sampling of the design space, until an error measure between the metamodel and the system has reached an acceptable level.
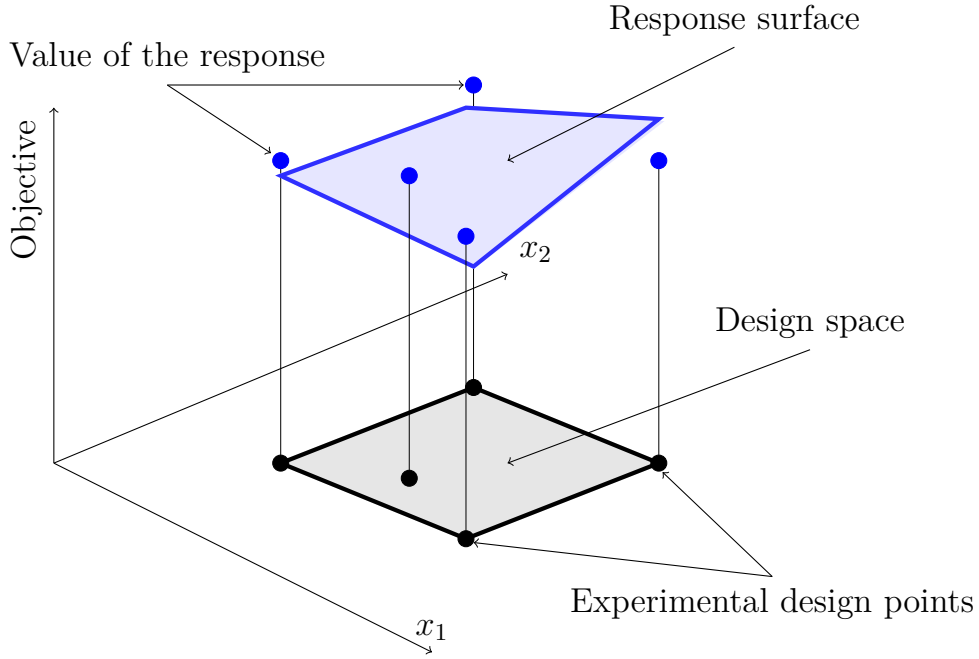
Figure 2.12: Response surfaces of a 2-D design space

The surface response method was chosen for this work for its computational efficiency and accuracy.

Chapter 3

Experimental Analysis

Summary

This chapter illustrates the experimental tests carried out during this work, describing the test specimens and the techniques used to acquire and process data.

3.1 Experimental samples

The first part of this thesis work was the retrieval of experimental data from the material samples that needed to be characterized. Seven different geometries of MS1500 martensitic steel were provided by *Centro Ricerche Fiat*. They completed part of the experimental analysis. Two out of the seven sample geometries were tested at Stuttgart *DYNAmore GmbH*'s laboratory. Figure (3.1) shows the seven different types of specimens tested. Each specimen will be referred respectively, from left to right, *shear 0°*, *shear 45°*, *notched*, *double notched*, *mini* and *big*.

Figure 3.1: Schematic of the different MS1500 tested specimens

The other material available was a DP800 dual phase steel, of which only two geometries were available. The figures (3.2) and (3.3) present the two types of specimens provided by FCA.
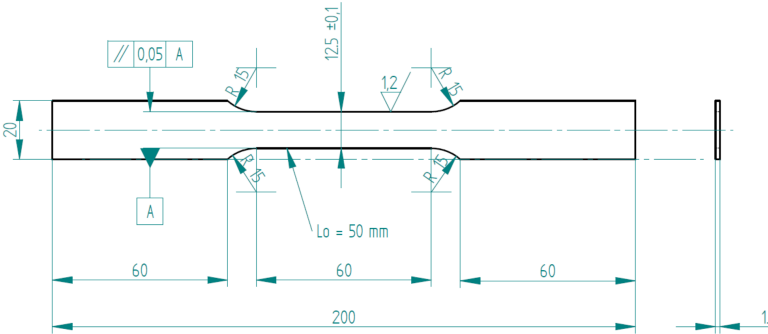
Figure 3.2: Schematic of the DP800 big_{dp} specimen

38
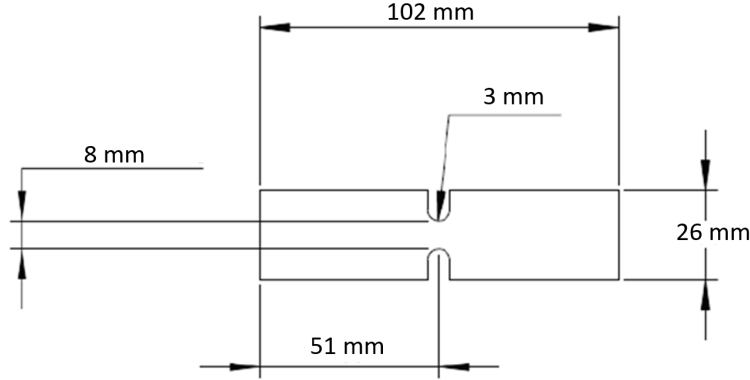
Figure 3.3: Schematic of the DP800 $notched_{dp}$ specimen

The characterization of the materials was carried out in two parts: yield curve and failure prediction.The main parameter that characterizes the stress state in failure modelling is the triaxiality [10]. The 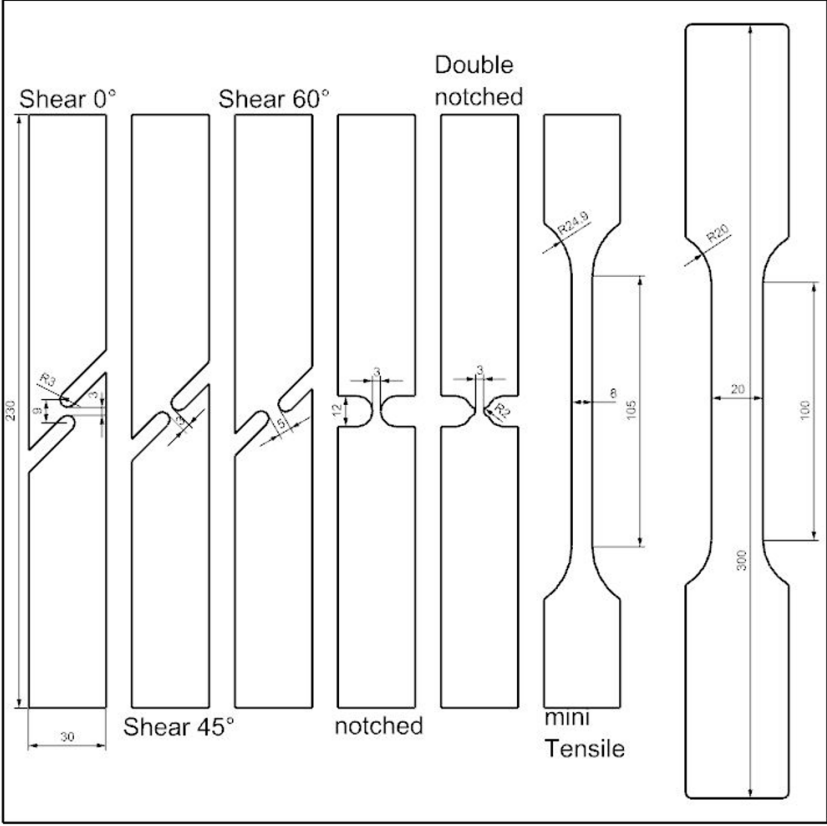objective of the characterization is to achieve a material model with predictive capabilities on a wide range of applications, geometries and loading conditions. To obtain an adequate material model the test specimens need to span the same triaxiality range. It is not reliable to predict material behavior for triaxiality values that were not tested. In the case of the MS1500, the seven different geometries subject the material to distinct stress states and achieve the needed triaxiality variability. The lack of some geometries for the DP800 steel has limited the possible analysis on it to just the first part: the determination of the yield curve. Chapter (5) explains in detail how the yield curve was determined for both materials.

All the samples were tested using a universal testing machine, UTS, which recorded the axial load with a load cell. Strain measure was carried out by digital cameras which recorded the portion of the specimen where the fracture was expected to occur. Stuttgart's laboratory test setup is shown in figure (3.4).
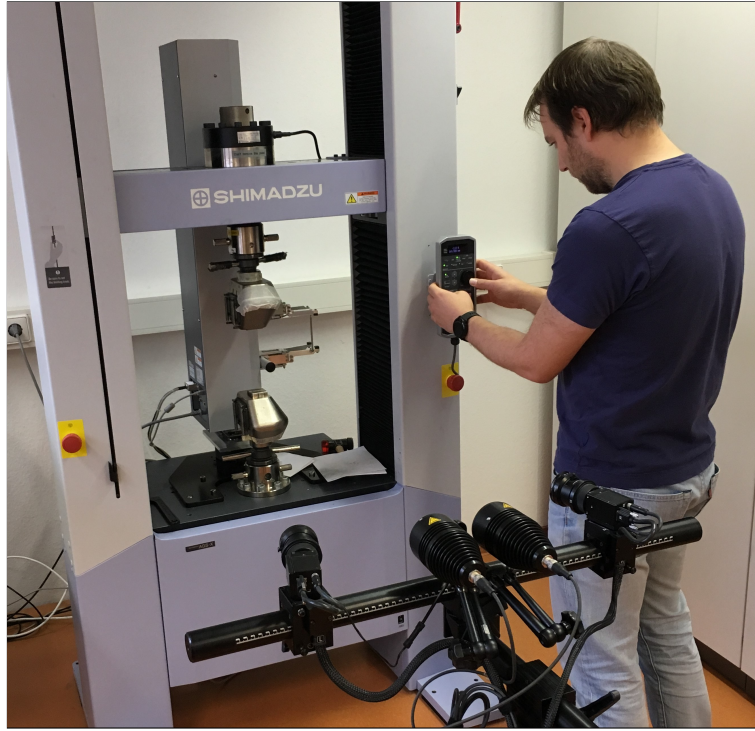
Figure 3.4: Testing setup in Stuttgart

The camera position is quite important for the correct result extraction. If one camera is used, it must be placed orthogonal to the plane of the test piece. If two or more cameras are used they must be parallel to the test specimen. Once placed, the cameras need to be calibrated. A picture of an object of known size, like a measuring stick, is used to record the size of the pixels. The object used for the calibration must be placed in the same position as the test specimen. This procedure allows for the conversion of pixels to numerical measures.

After each test, load and displacements data has to be synchronized, since the UTS' sampling rate is different than the frame rate of the cameras. The synchronized data is input into the DIC software *GOM*, and a region of interest (ROI) is created by selecting the part of the test specimen with

the highest deformation concentration. The ROI is meshed with triangular elements and six of them make a facet. Figure (3.5) shows the ROI with the triangular mesh. The size of the facets is crucial for comparing the measured
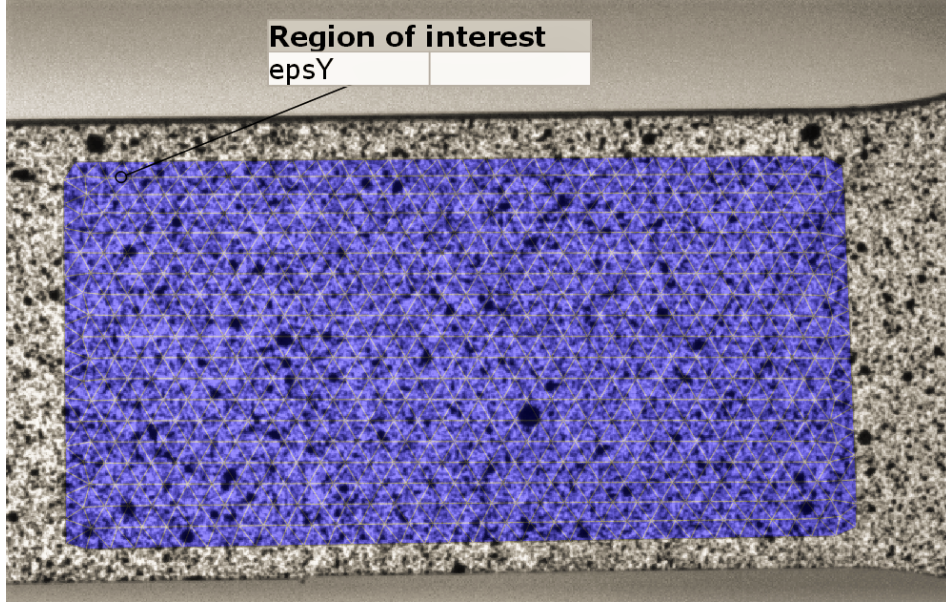
Figure 3.5: ROI and triangular mesh

strains to simulated strains. The DIC software calculates strains based on a characteristic length l_0 which is proportional to the facet size, shown in figure (3.6). The FEM simulation's mesh size used to reproduce the experiment
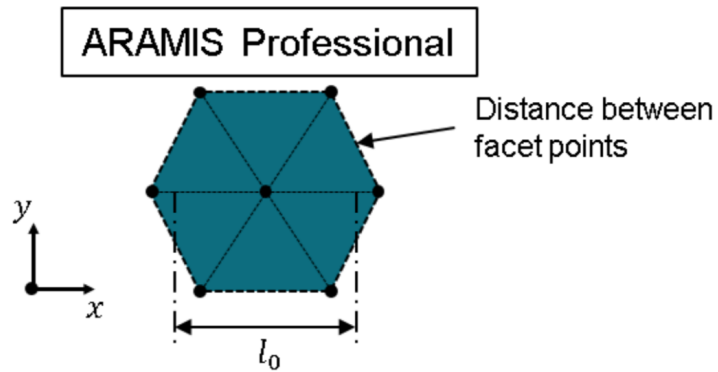
Figure 3.6: Facet with reference length

must be comparable with the mesh size selected in the DIC software [13] to directly compare results. A difference of more than an order of magnitude between l_0 and the simulation's characteristic length could yield questionable results [13].

Each geometry was tested 3 times for the repeatability of the measure and the average calculated from the replicated tests was used in the following analysis. From every test two sets of experimental curves were extracted. The first kind comprised a force-engineering strain curve, as if the experiment was carried out using a traditional extensometer. This curve is extracted from the DIC software using a digital extensometer. The results for one of the specimens is shown in figure (3.7). The second curve type includes the force-
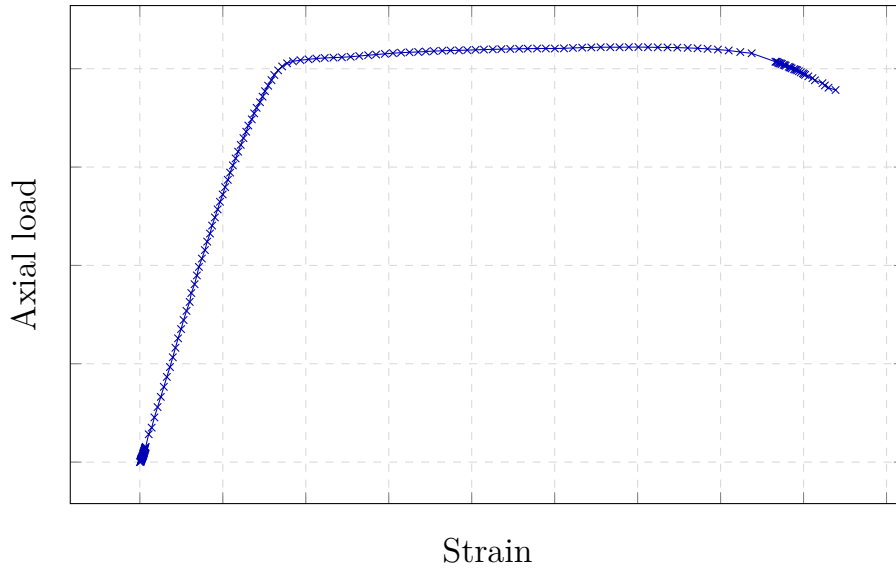
Figure 3.7: Axial load-engineering strain curve of the material, *big* specimen

true strain curves for each facet inside the ROI. The DIC software exports the axial force as a function of strain for each facet, generating a hyper-curve. An extracted hyper-curve example can be seen in figure (3.8). It is
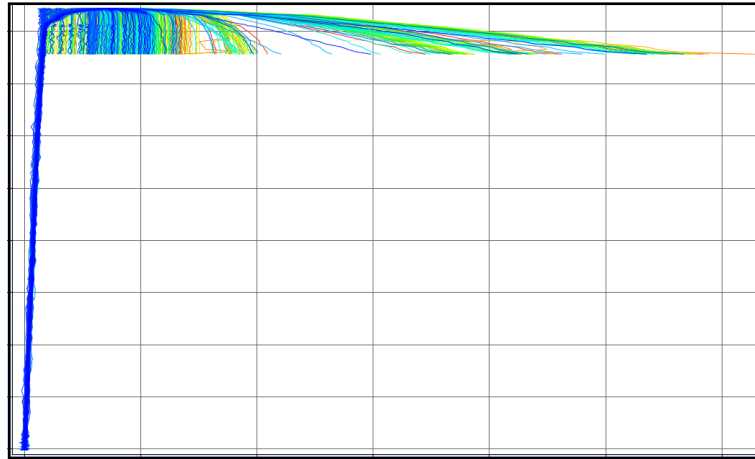
Figure 3.8: Load strain curves extracted with the DIC

a collection of force-strain curves calculated in different locations using the same load. Points that are close to the strain peak result in a curve more stretched. Points that are further away behave almost elastically.

To achieve proper correlation of the displacements the specimens were first sprayed with white paint, and then after a short time with black paint. The black paint must be applied from a distance to achieve a uniform distribution of black marks. The average size of the marks should be 3 to 5 times bigger

Figure 3.9: Sprayed test specimens

than the image's pixel size, the pattern is shown in figure (2.6). Speckles that are too small result in suboptimal contrast, and too large speckles reduce the measurement resolution [14].The quality of resulting patter, in figure (3.9), was verified with the DIC software and no issues were found.

The results of the two DP800 tensile tests are presented below in figure (3.10).
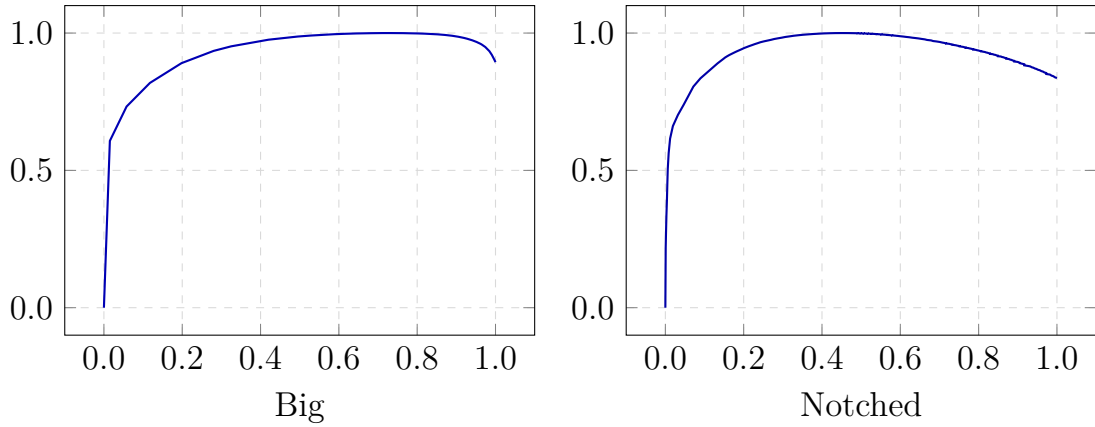
Figure 3.10: Normalized axial force-engineering strain curve of the DP800 specimens

The results of six of the MS1500 tensile tests are presented below in figure (3.11). The results for the shear 0° specimen were unusable because the field of view was too narrow for the extraction of strains. The experiment was carried out with the camera placed too close to the test specimen due to the test machine geometric restrictions, so only one side of the specimen could be seen. Both sides of the specimen must be visible in order to extract usable data.
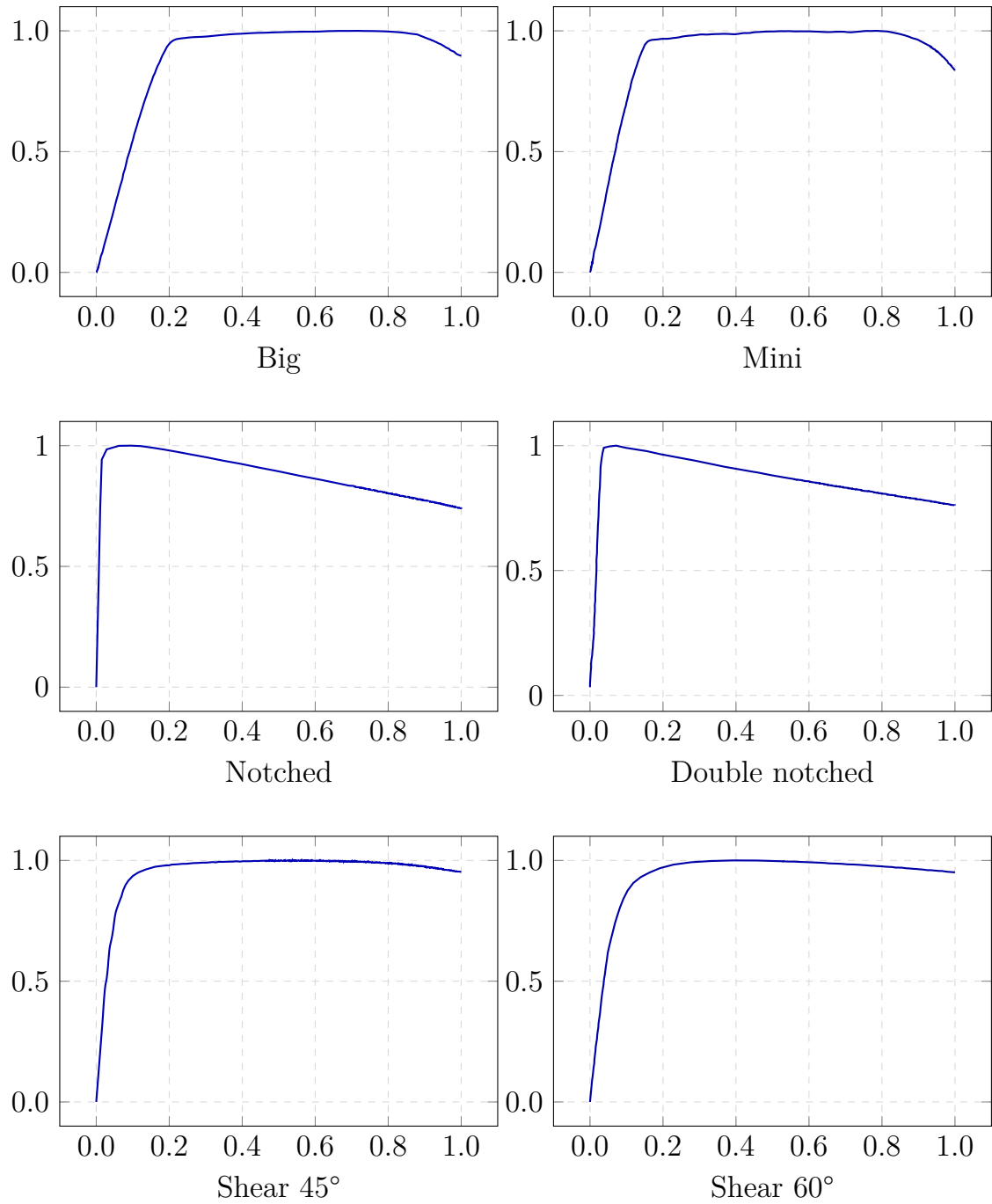
Figure 3.11: Normalized axial force-engineering strain curve of the different specimens

Chapter 4

FEM models

Summary

This chapter explores the simulation of the test specimens using the finite element software LS-DYNA. Chapter 4 begins by exploring the topic of mesh generation and goes on to explain the thought processes behind selection of the material model, the element formulation, the boundary conditions and the model deformation. This chapter ends describing and illustrating the analysis of the simulation results.

4.1   LS-Dyna

There were 2 available test specimens for the dual phase 800 steel, and 6 for the MS1500 martensitic steel. The DP800 was included only in the yield curve analysis due to the lack of specimens. Having the MS1500 in dif ferent geometries also allowed for the study of its failure. To simulate the experimental analysis the geometry of each specimen was reproduced inside a CAD

software and the resulting geometry was loaded into LS-PrePost to generate a mesh. The elements were created with sides of 0.5 mm in the critical area of each specimen, located where the fracture is expected to happen. The mesh became gradually more coarse as distance from these areas increased. The minimum size was chosen to avoid spurious mesh dependencies in the damage model used in the simulations [13]. Elements that are too big struggle to describe a physical phenomena such as cracking or fracture because they occur on a smaller scale than the mesh's characteristic length.

The damage model selected for the MS1500 study is the Generalized Incremental Stress-State dependent Damage Model (GISSMO)[15]. To make the results of this work applicable to a crash simulation the GISSMO model provides a regularization parameter that can be tuned to make the results independent from the mesh size. The regularization is crucial because in a crash analysis the average size of the elements is usually 5-6 mm. The tuning of the GISSMO model will be discussed in Chapter 6.

For the MS1500, only four of the six available experiments were used in the GISSMO optimization because the *shear 60°* simulation behaved differently than the measured physical sample and the and *mini* was incompatible with the *big*. This discrepancy probably arose due to the simple material model selected for the simulations; more details on this matter are in section (4.1.1). Additionally, The test material on the ultra high strength martensitic steel could have some orthotropic properties that are not considered in the material model. This could also lead to the incorrect *shear 60°* simulation. The fifth and the sixth specimens were used as control, but they were not used in the computation of the material parameters. The figure (4.1) shows the 5 simulated geometries:

48
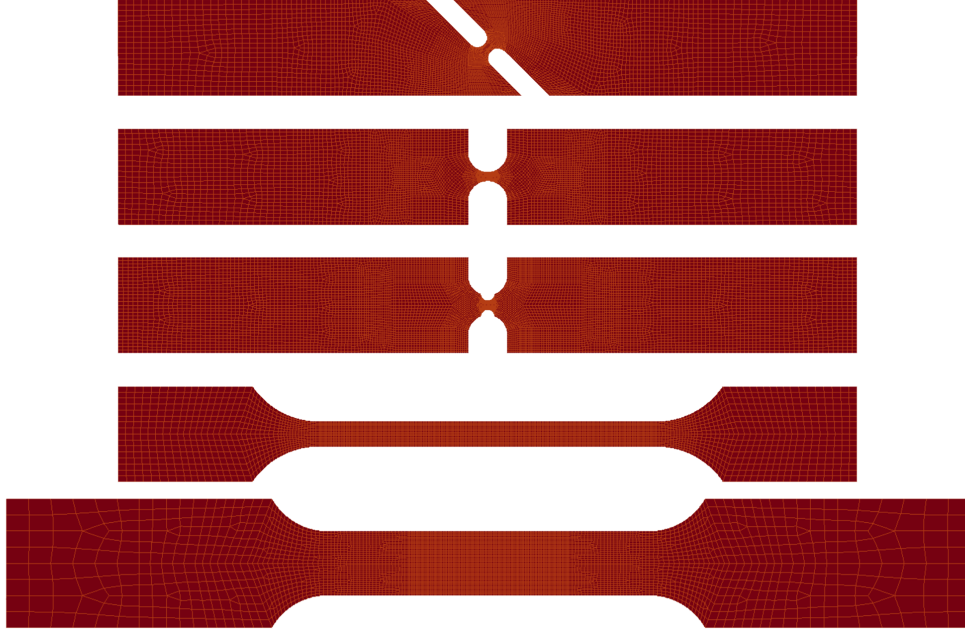
Figure 4.1: The meshed geometries, respectively from top to bottom: *shear 45°, notched, double notched, mini* and *big*

For the DP800 the two geometries were simulated but, since the GISSMO model optimization was not performed, only big_{dp} was used to tune the yield curve. $Notched_{dp}$ was used to verify the result of the yield curve. The meshed geometries are presented below in the figure (4.2)
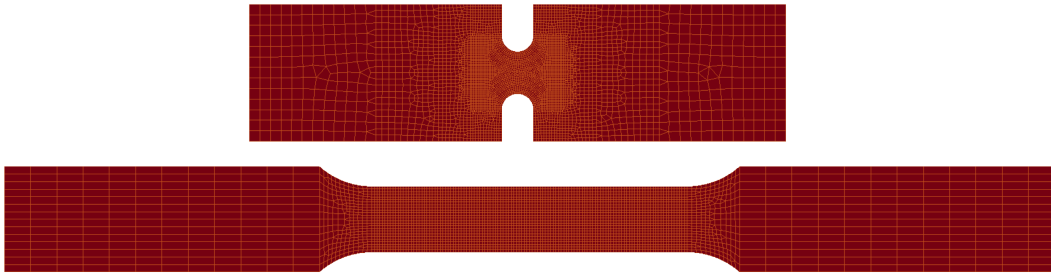
Figure 4.2: The meshed geometries, respectively from top to bottom: $notched_{dp}$ and big_{dp}

4.1.1 Material model

The material model chosen for the simulations was, in the LS-DYNA keyword notation, *MAT_PIECEWISE_LINEAR_PLASTICITY[16]. This model was chosen because it is one of the most used material models in the crash analysis thanks to its balance among computational efficiency, simplicity and accuracy in the results. The model chosen is also an elasto-plastic material model with the potential to define an arbitrary stress-strain curve[16] as a constitutive relation, which allows for the simulation of a wide range of materials. The stress-strain curve required by the model must be a true stress and true plastic strain curve. This is referred to as *yield curve.*
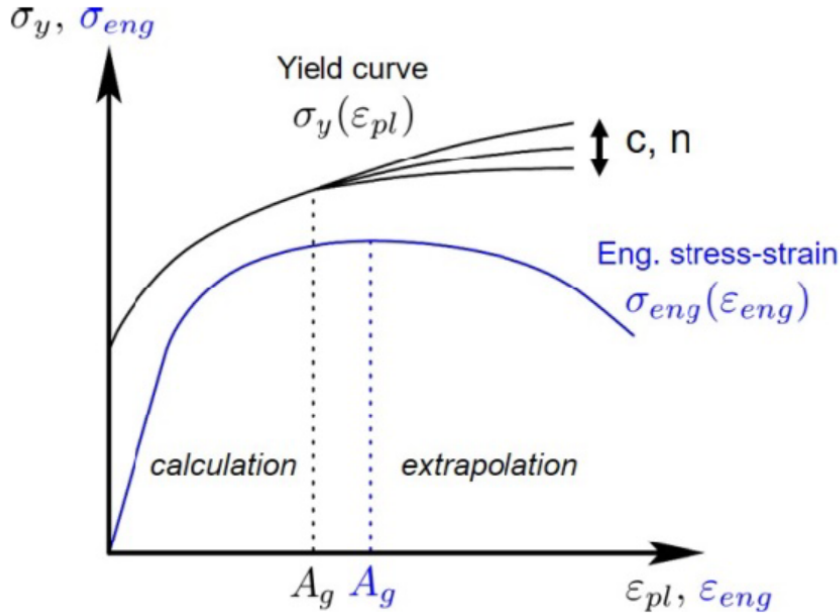
Figure 4.3: Yield curve extrapolation compared to the corresponding test results[13]

To obtain the yield curve shown in figure (4.3), the test results of the *big* specimen were processed as described in section (2.1). The true strain was calculated using the measured engineering strain and the equation (2.5).

Then the plastic strain was obtained by subtracting the elastic strain to the true strain, as in the equation (4.1).

$$\epsilon_{pl} = \epsilon - \frac{\sigma}{E} \tag{4.1}$$

Obtaining the true stress requires two phases. True stress can be calculated with the equation (2.7) until the point of uniform elongation. Then a plasticity model is introduced to calculate the true stress after the point of uniform elongation because the stress state is no longer uniform and the cross-section no longer constant. The Hockett-Sherby model described in the section (2.2) was used in a modified form. It presents two free parameters that must be optimized to the material's behavior. Their determination is described in the Chapter 5. The model's equation is:

$$\sigma = A - B \cdot e^{\left(-C \cdot \epsilon_{pl}^{N}\right)} \tag{4.2}$$

C and N represent the two free parameters, because A and B are bound due to the requirements of C1 continuity in the transition from uniform to non uniform elongation [13]. By iteratively choosing C and N until the experiment behavior is found in the simulations, the material is characterized. The material model handles plasticity using a Von Mises Yield surface based on a J2-plasticity[13].

4.1.2 *MAT_ADD_EROSION

Another material card was added to the simulation to simulate the failure. In the LS-DYNA keyword notation, the *MAT _ADD_EROSION card permits users to introduce the GISSMO model of damage accumulation into the simulation, allowing users to modify the damage occurrence and the fracture speed. This damage model is highly modular and can be used with many of LS-DYNA's material models. The GISSMO's most important modifiable parameter is the damage accumulation rule[15]:

$$\triangle D = \frac{n}{\epsilon_f(\eta)} \cdot D^{\left(1-\frac{1}{n}\right)} \cdot \triangle\epsilon_{pl} \tag{4.3}$$

in which the free variables are n, the damage exponent, and $\epsilon_f(\eta)$, the fracture strain as a function of the triaxiality. Using the current values of the damage D, of the plastic strain ϵ_{pl} and of the triaxiality η equation (4.3) is evaluated in every time step of the simulation and the damage is accumulated. D starts from 0 for every element in the simulation. When the damage in one element reaches unity the considered element is deleted, as it is unable to bear stress. The possibility to change the value of the damage exponent n allows for a non linear accumulation of the damage. Values of n higher than 1 accumulate damage slowly at the beginning and accelerate the process as D approaches 1. Values lower than 1 present the opposite behavior.

Another useful aspect of GISSMO is the introduction of coupling between the damage and the stress in the element. Damaged elements can withstand less stress than elements without damage. The coupling enables the description of the weakening of the elements. It is implemented in the model with an instability parameter F and its accumulation rule is similar to the equation

(4.3):

$$\triangle F = \frac{n}{\epsilon_{crit}(\eta)} \cdot F^{\left(1-\frac{1}{n}\right)} \cdot \triangle\epsilon_{pl} \tag{4.4}$$

with the difference being that $\epsilon_{crit}(\eta)$ is the moment at which the plastic damage starts influencing the stress. When F reaches 1 coupling starts:

$$\sigma = \tilde{\sigma} \cdot \left[1 - \left(\frac{D - D_{crit}}{1 - D_{crit}}\right)^m\right] \tag{4.5}$$

$\tilde{\sigma}$ is the stress that would be present in the element without damage and it is reduced using the equation (4.5) to obtain σ, what is actually present in the damaged element. The stress scaling is done using the current damage (D), the damage at the time step when F reached 1 (D_{crit}), and the so-called fading exponent m, which is a characteristic of the material and it has to be calibrated [15].

The curves describing the material's dependency on triaxiality of ϵ_{pl} and ϵ_{crit} together with the two accumulation rule's exponents, n and m are the objectives of the optimization carried out in chapter 6. The correct combination of these parameters simulates the material behavior.

4.1.3   Element formulation

All the FEM models were generated using fully integrated quadrangular shells, formulation 16 inside LS-DYNA[16]. Strain along the thickness was taken into account to enhance precision and 5 integration points through the thickness were selected.
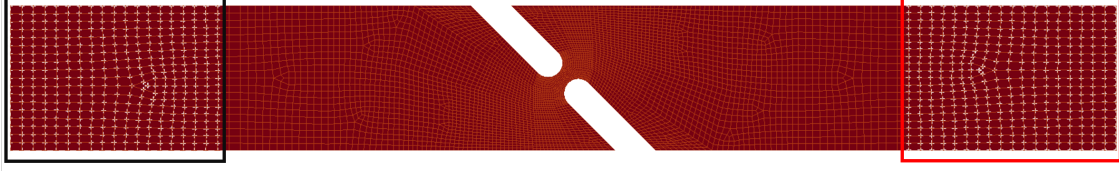
4.1.4   Boundary conditions

Figure 4.4: Shear 45° model with the constrained nodes highlighted

The models' boundary conditions were designed to reproduce the experimental tests. Figure (4.4) shows one of the models highlighting the applied constraints. The nodes with white markers surrounded by a black box on the left side are constrained in all six degrees of freedom to reproduce the UTS' fixed clamps. On the opposite side the nodes surrounded by the red box are free to move only along the x direction. All the non highlighted nodes are not constrained. The same logic was applied to the other models in preparing the boundary conditions.

The load was applied on the constrained nodes on the right side through controlled motion. A displacement curve function of time dictated their movement. The curve relative to the shear 45° specimen is presented in the figure (4.5). This definition results in constant speed and acceleration for the duration of the simulation, except during the transient phase at the beginning. For this reason kinetic energy levels were monitored in all the simulations: the ratio of kinetic over internal energy did not exceed $10 - 15\%$ in the transient. For the rest of the duration of every simulation, roughly 90%, it stayed below $3 - 7\%$. The deformation speeds chosen for the simulations were higher than those experienced by the test specimens, as the tensile tests are carried out in quasi-static loading conditions. The simulation's higher displacement speed, which evidently increases the deformation rate,
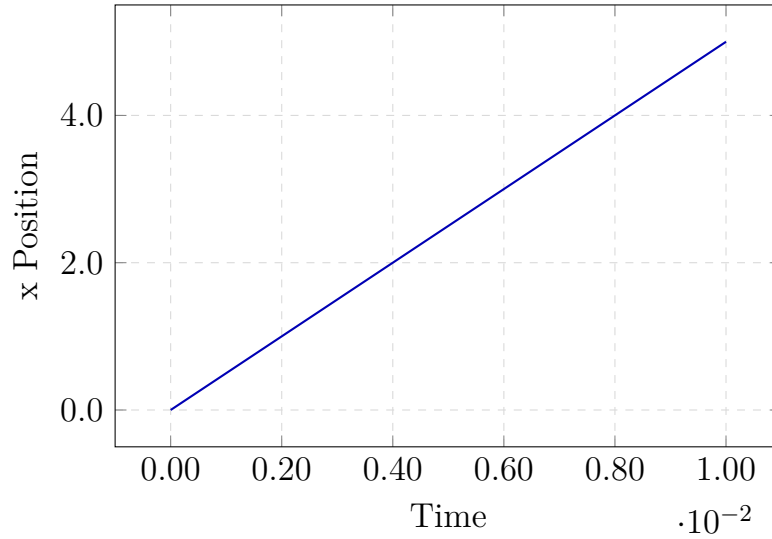
Figure 4.5: Shear 45° model prescribed motion curve

is needed due to the size of the mesh and the type of solver utilized. The mesh size influences the maximum valid time-step for the explicit solver and, even taking into account some mass scaling, the computational time associated with reproducing the same strain rate would have been unreasonably long. In this work the strain rate influence on the material properties was not taken into account. Having the simulation run at higher strain rates is an acceptable compromise to reduce the computation times.

4.1.5 Solver

The solver used in this work is LS-DYNA's explicit method. This method was chosen because the results of this work are thought to be used in crash simulations, which are run explicitly because of the high deformations and the high deformation's rate reached in the car models. The computation time was mainly influenced by the size of the smallest elements in the mesh.

The introduction of mass scaling allowed for some time step increase. It was limited to 2% of added mass[16].

4.1.6   Results extraction

The aim of this work is to compare the effectiveness of different calibration methods: traditional that uses just the data from an extensometer and full field calibration, which analyzed a portion of the strain field. To do this, two sets of results were obtained from the simulations. For the traditional optimization, the axial load and the displacements of two nodes were recorded, where the two nodes represented the extensometer measuring points in the simulation. The figure (4.6) shows one sample geometry and the position of the nodes where the displacements are recorded. The location of the two nodes is different in every specimen and reflects the placement of the extensometer in the experimental test. A load engineering curve for each
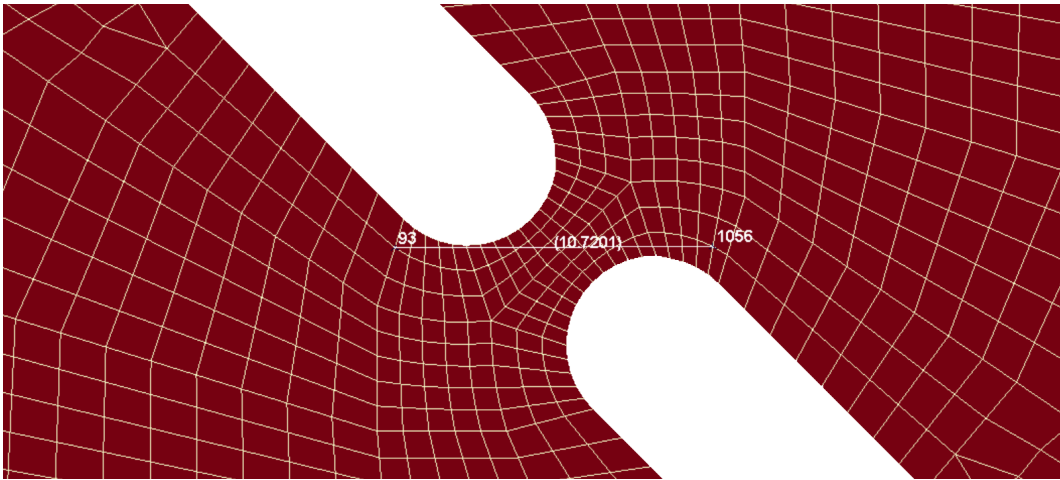
Figure 4.6: *Shear 45°* specimen with its nodes where the displacement is measured highlighted

simulation was evaluated as the difference of displacement along the x direction of the two selected nodes. This curve is used to rate the parameters' accuracy in each simulation in the traditional optimization cycles.

The second type of results extracted comprised of the same axial load and strain field, which is recorder in LS-DYNA inside the *d3plot* files. A collection of curves comparable to the experimental hyper-curves is obtained by combining the load and the strains. It is a collection of the force strain curves calculated on the elements of the model that fall inside the ROI of the corresponding experiment. An example is presented in figure (4.7). This object is used to evaluate the accuracy of each simulation in the full field optimization.
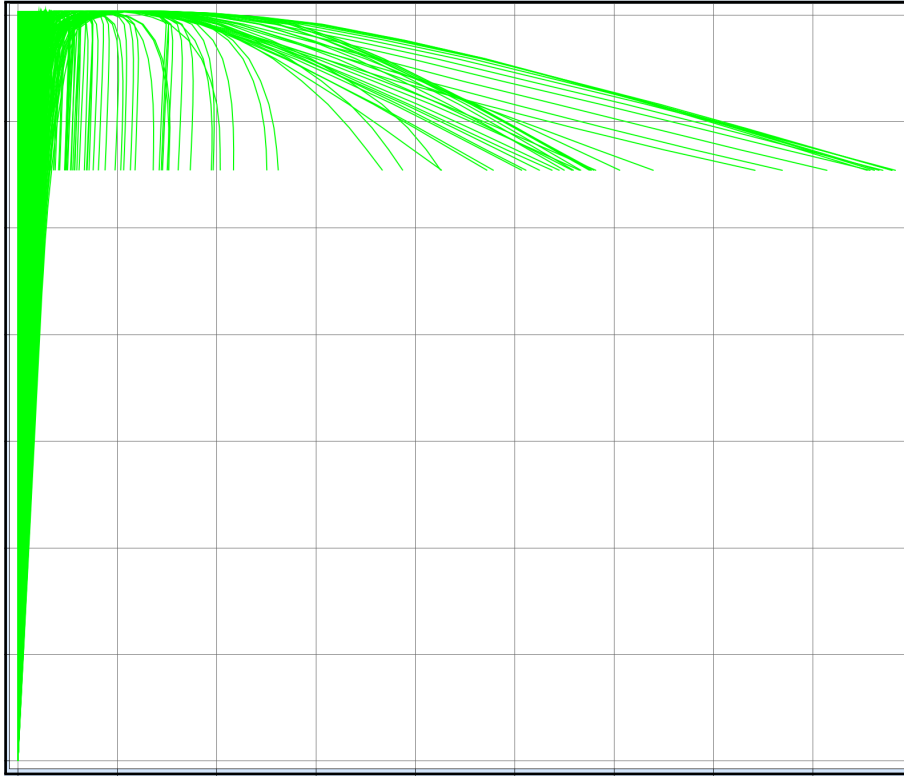
Figure 4.7: Multi-point force strain curves

Chapter 5

Yield curve optimization

Summary

This chapter will report on the optimization problem formulation for the determination of the material yield curve for the two steels (MS1500 and DP800). At the beginning the input files are prepared for the simulations. In section (5.2) two optimizations are prepared, one in the traditional way and the other using the full field calibration method for both materials. In Section (5.3) a third yield curve is generated following the Volume conservation (VC) approach. The simulation results for each yield curve are then compared to the experimental data in Section (5.4), both looking at and engineering stress strain curve and at the strain field, to evaluate the effectiveness of the three methods. In Section (5.5) the same process was also followed for the DP800 steel to verify the procedure with a more ductile material. At the end of the chapter the results are discussed.

5.1 Input file preparation

The objective in this phase is to obtain the MS1500 and the DP800 yield curves for the *MAT_PIECE- WISE_LINEARITY card. The two optimizations for the first two yield curves was carried out twice using LS-OPT in combination with LS-DYNA. For the Volume conservation method no optimization was run, as the yield curve can be calculated directly. A more complete description is in Section (5.3). The optimal curve would result in a overlap between the force-engineering strain curve extracted from the experiment and the one resulting from the FEM simulation. For the optimizations LS-DYNA and LS-OPT work together tightly through the use of the *PARAMETER card. All the numbers in the input files can be parametrized using said card and LS-OPT is able to recognize the presence of a parameter and change it during the simulation steps.

To obtain the yield curve in the optimizations only one of the tensile tests per material was analyzed. For the MS1500 the *big* specimen was analyzed, for the DP800 the big_{dp}. Their input file were modified to let the optimization perform the simulations changing the yield curves, until the optimal one is found. The chosen structure was having part of the yield curve fixed, up to the point of uniform elongation, and the rest variable. The variable part was modeled with the H&S equation and was calculated at the beginning of every simulation by LS-DYNA with the values of c and n that LS-OPT provided. The two parameters were in the *PARAMETER card so that LS-OPT could modify the yield curve. Then, the two LS-OPT projects were created.

5.2   LS-OPT optimizations

Both of the standard and FFC optimization projects shared the same structure and approach, with some difference in which parts of the simulations results (*responses*) were analyzed and compared to the desired mechanical behavior. The final structure of the optimization was determined through trial and error.

The problem of finding the values that characterize a material is known as parameter identification. The LS-OPT manual suggests for these problems the formulation of the optimization using a metamodel and a sequential with domain reduction (SRSM) strategy. Initially a linear metamodel was used. This approach is suggested because the objective is finding just one pair of values in the design space, not obtaining an accurate description of the global behavior of the model. To find the optimal combination of parameters the optimization gradually reduces the size of the design space until the linear model can accurately reproduce the experiment's behavior. Unfortunately the results with this approach were not satisfactory enough. The reduction of the domain was excluding the optimal parameter values and remained stuck in local minima. Changing the size of the design space was attempted and resulted in better match between experiment and simulation, but the correspondence was still insufficient so another approach was tried.

The use of feed forward neural networks (FFNN) to generate the metamodel yielded a better match. The different type of metamodel resulted in a change of optimization strategy, which was changed to a sequential optimization. In this case the design space remained unchanged and more points were added each iteration to enhance the accuracy of the metamodel. The

sequential optimization is a global optimization strategy, as it approximates the model behavior in the whole design space with the FFNN, while the SRSM strategy reduces the design space until the linear model is accurate enough. Figure (5.1) shows the comparison between a linear metamodel with
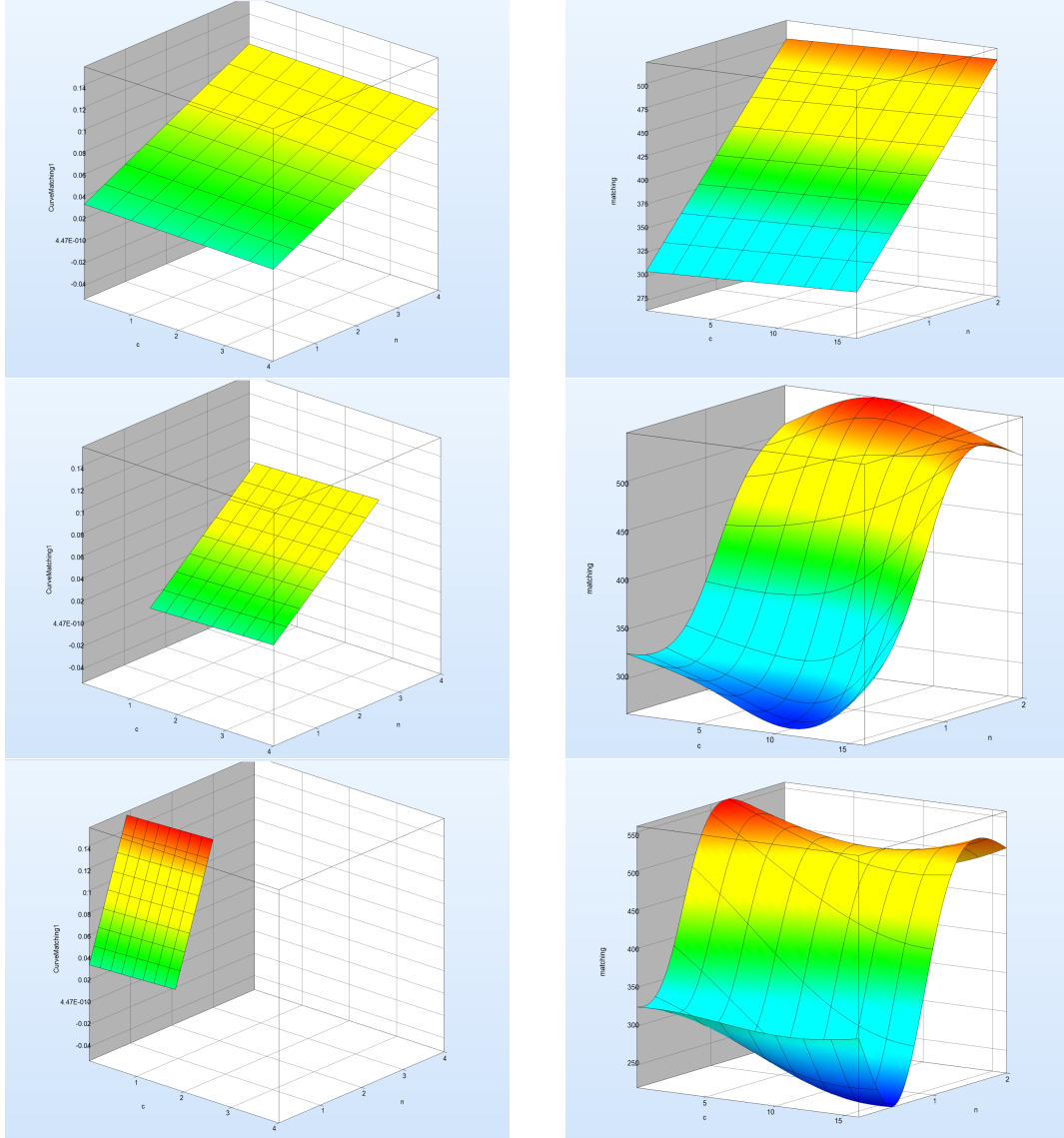
(a) Linear Metamodel with SRSM   (b) FFNN and sequential opt.

Figure 5.1: Global and local metamodel generation strategies

SRSM strategy and a more complex metamodel, generated with FFNN with

a sequential strategy. The images on the left highlight how in the SRSM strategy the design space is reduced after each iterations so that a simple linear model can reproduce, in the reduced design space, the modeled phenomena with accuracy. The ones on the right show how using FFNN the metamodel starts simple, but becomes more complex with the addiction of more simulation points and in the end is able to accurately describe the whole design space. Both strategies have strength and weaknesses depending the application. A global optimization was chosen to enhance the results, at the expense of the computation times because global approximations need more iterations. Also, the use of FFNN metamodels generally require more iterations than linear metamodels to get the same accuracy[12].

Using FFNN and the sequential optimization strategy resulted in the LS-OPT project shown in figure (5.2):
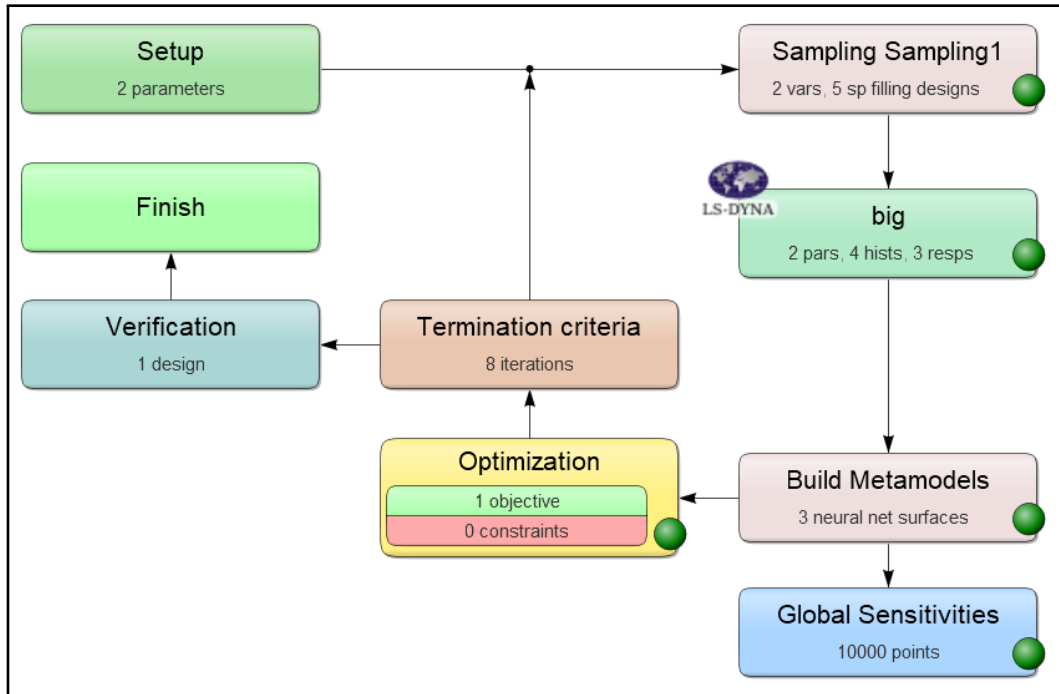

Figure 5.2: LS-OPT project structure

63

Figure (5.2) shows the steps the LS-OPT follows every iteration of the optimization. First, the free parameters are selected, top letf corner of the figure, and the design space is generated using the upper and lower bounds of the free parameters. Then, LS-OPT samples the design space, which means chooses what points to evaluate in the simulation stage that follows. Different sampling strategies can be selected. For the FFNN metamodel the suggested strategy is called *space filling*. It, given a number of points to evaluate inside the design, tries to keep them all as far apart from each other as possible. This strategy "fills" the design space trying to extract the maximum amount of information about the global behavior of the model with the least amount of points.

The points selected by the sampling algorithm are then utilized to run a number of simulations. The number of points per iteration is proportional to the number[12] of free parameters and it is determined with equation (5.1):

$$n = (1.5 \cdot (i + 1) + 1) \tag{5.1}$$

where n is the number of design points per iteration and i is the number of free variables. If more geometries are presents n is the number of simulations per iteration per geometry.

Using the responses of every simulation the current iteration's metamodel is built. The responses are the axial force and the strain along a fixed length, which are compared with the corresponding experimental result to compute a match score. The metamodel then is searched for the minimum of the matching score and using the expected minimum a verification simulation is run. The responses coming from the expected minimum are compared with the experimental values to evaluate the metamodel's accuracy. If the

accuracy is inside the selected interval the optimization is concluded and the optimal combination of parameter is found. Otherwise another iteration is performed following the steps discussed previously, until the desired accuracy is reached in the metamodel and the material parameters are available.

5.2.1 Traditional yield curve

The first optimization had as objective the axial force-engineering strain curve measured on the *big* sample with a gauge length of 80 mm. The corresponding strains were read from the simulation, recording the displacements of two nodes 80 mm apart and the axial force during the simulation. To confront the two curves LS-OPT presents a collection of matching criteria, in this work the *dynamic time warping* was used. It was chosen because it performs well with the type of curves that usually result from tensile tests of steels. For further explanation on the matching algorithm refer to the LS-OPT user manual. The criteria requires the two compared curves to be the same length, so before the evaluation the curves extracted from the simulations were cut at the last recorded experimental load.

5.2.2 Yield curve through full field calibration

The other optimization problem had as objective the hyper-curve extracted from the tensile test footage of an area surrounding the fracture. It is not necessary to include the whole piece in the ROI, point too distant from the strain localization area do not contribute to the analysis. The hyper-curve consisted in axial force-true strain curves, and for the MS1500 specimen 670 of them were present. The corresponding curves were extracted from

the simulations reading the *d3plot* files that LS-DYNA generates and the matching was done using the same criteria, cutting the curves at the force value that was measured last in the experiment.

The full field calibration requires one intermediate step before the matching is possible. The FEM model and the mesh generated by the DIC software are most likely created in different reference frames. They must be aligned properly before any comparison can be done. LS-OPT provides the necessary tools to do it, but as of this writing some manual work is still necessary. A transformation must be formulated to align the two meshes. To generate it a minimum of three nodes from each model that should be coincident when aligned must be found. The coordinates of the selected nodes must be recorded and LS-OPT generates a transformation that moves the nodes from the experimental mesh on top the corresponding simulation nodes. The alignment used for the MS1500 optimization is shown in the figure (5.3) and the figure (5.4) as an example:
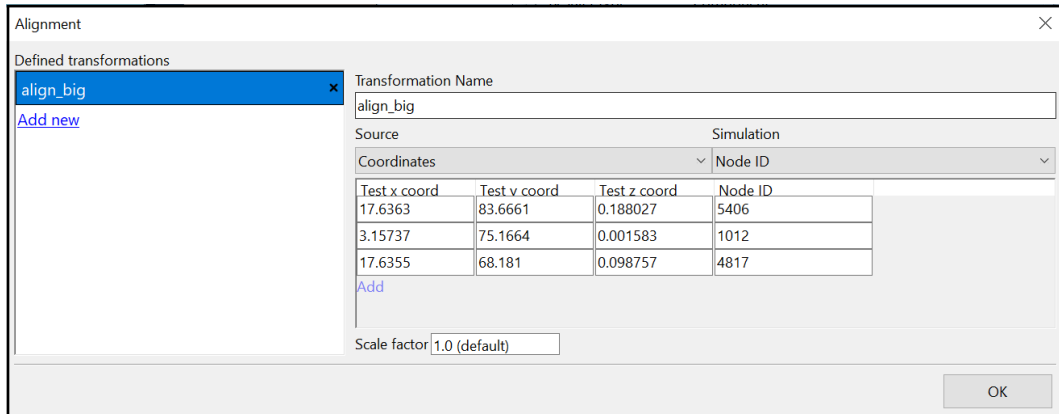
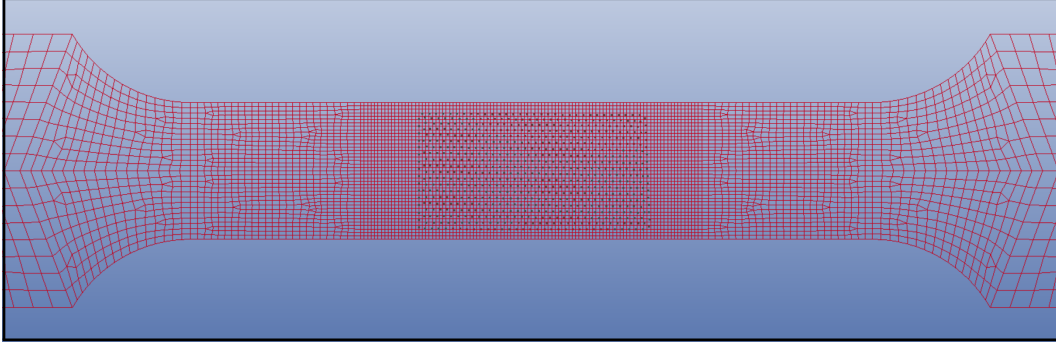

Figure 5.3: LS-OPT alignment screen

Figure 5.4: LS-PrePost alignment screen. The mesh is presented in red while the black dots represent the facet centers.

5.3 Volume conservation method's yield curve method

The third yield curve was generated following the approach of Section (4.1.1) with some differences. The strains were measured in the area of highest strain concentration, taking into account the peak value and with a much shorter gauge length. This highly local measurement was possible thanks to the DIC. Due to the quite small measurement area, the hypothesis of conservation of volume and uniformity of the strain field can be assumed valid. This allows to use equation (2.7) to calculate true stress up to the failure of the specimen, without needing any optimization. The curve was extended using a a linear fitting function to include strains up to $\epsilon = 2$. Only one simulation with this yield curve was performed.

5.4 MS1500 Steel yield curves

The yield curves results of the two optimizations and of the "VC" method are presented in figure (5.5). The ones resulting from the optimization appear
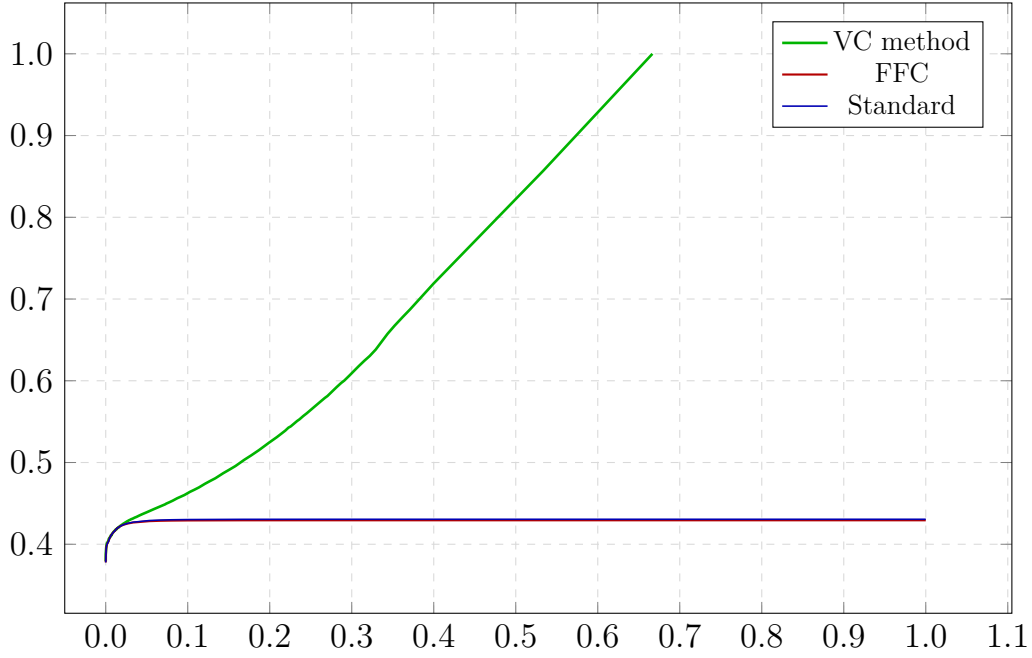
Figure 5.5: MS1500 yield curves comparison

quite similar in shape, with the one found by the FFC method being much steeper. The curve calculated with the VC method at the beginning stays with the other two, but around the yielding point proceeds to diverge to a much stiffer behavior. The normalized experimental axial force-engineering strain curve is compared with the corresponding curves resulted from the simulation of the three yield curves in figure (5.6). All three models nicely reproduce the material yield, though they all present a delay in the initiation of the localization of the strain. The "VC" one presents a much more ductile behavior, while the other two reach failure coherently with the experiment. The VC simulation continued deforming much further the values registered in the experiment and presented a different strain localization locus. Failure prediction was not the objective of this comparison and in fact besides this
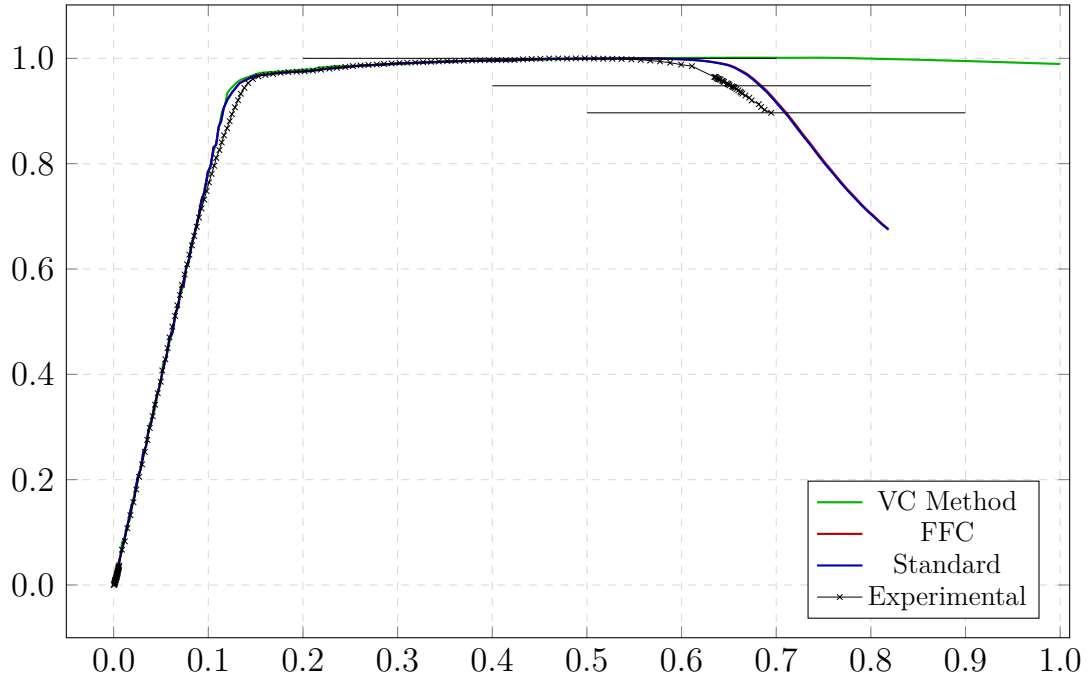
68

Figure 5.6: MS1500 engineering curve comparison

difference all the models were matching the experiment's force-engineering strain curve very accurately. More differences were found inspecting the strain fields generated in the three models and comparing them to the one measured during the tensile test. Figure (5.7) shows the strain fields of the experiment compared with the fields of the three models at three different force levels: when necking begins and two afterwards. The load level of the three comparison points is shown in figure (5.6) with three black lines.

The first comparison point, first line of pictures, highlights the delay in localization of the strain that was observed in the force-strain curves above. The following two show how each yield curve influences the localization of the strains. Both the "FFC" and "Standard" model were able reproduce the slip plane on which the experimental sample experienced the fracture.
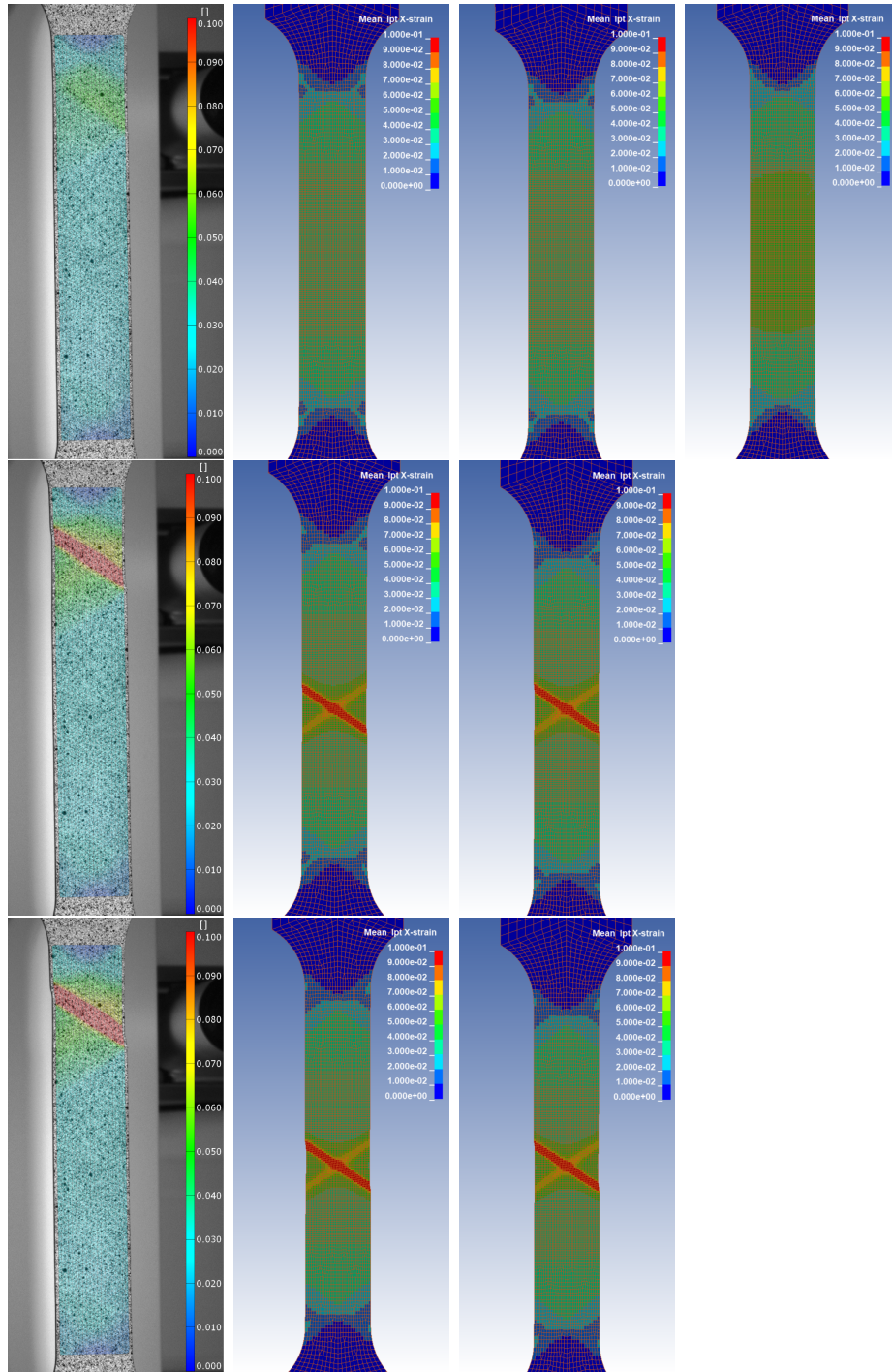
(a) DIC   (b) FFC   (c) Traditional   (d) VC

Figure 5.7: Strain field comparison

The "VC" model yields an acceptable force-engineering strain curve, but the material behavior is very different when compared to the others. It presents a more ductile behavior and the load registered in the simulation does not drop, making impossible a comparison of the strain field after the peak load. When the localization occurs it is comparable to the necking of a ductile steel. Figure (5.8) shows the "VC" strain field when this phenomenon is observable.
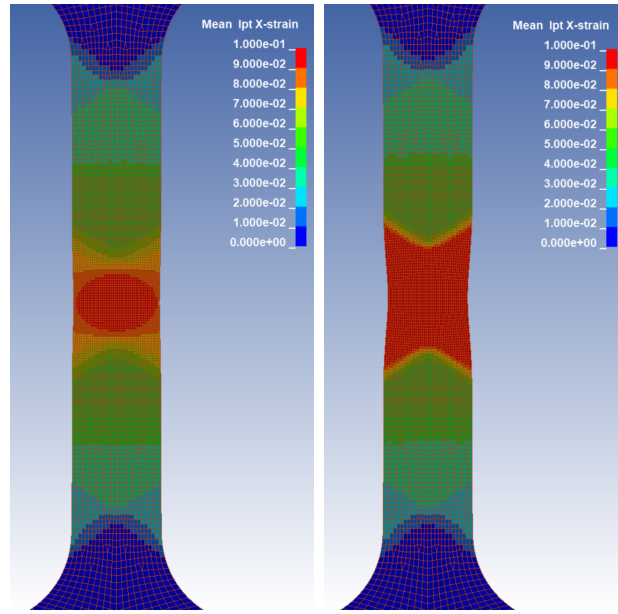
Figure 5.8: Strain field comparison at two subsequent time instants

Table (5.1) shows the maximum measured strains at the load levels of the Figure (5.7):

Comparison load	DIC	FFC	Standard	VC
Max. Load	0.052	0.0327	0.0338	0.0405
(Max. Load)·0.95	0.192	0.220	0.299	N.A.
(Max. Load)·0.9	0.313	0.358	0.373	N.A.

Table 5.1: Maximum measured true strain along the specimens length

The maximum measured strain highlights that the "FFC" model is able to more accurately predict the material behavior. The difference in the strains that arises after the necking is not negligible, but it was expected because in those conditions the material behavior is no longer isotropic and triaxiality dependent. Only a true stress-true strain curve cannot accurately portray the experimental strain field. This issue is addressed in the Chapter (6) with the introduction of the failure model GISSMO.

5.5 DP800 Steel yield curves

The same procedure was followed with a sample of a dual phase 800 steel. One specimen was tested inside FCA's laboratories and the footage of the tensile test was analyzed. Three yield curves were generated using the aforementioned approaches and the results compared to the experimental tests. Figure (5.9) shows the yield curves that resulted from the analysis.
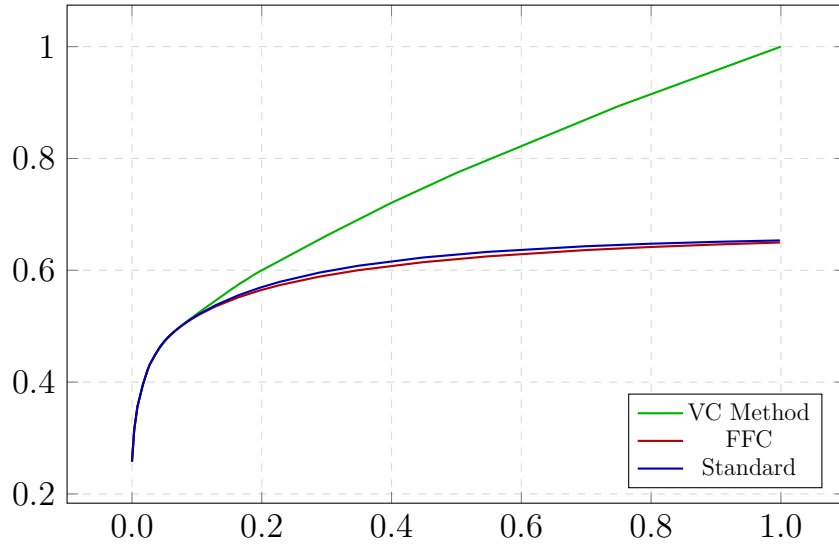

Figure 5.9: DP800 yield curve comparison

The simulation results are plotted below in figure (5.10), which shows the normalized axial force-engineering strain curves of the experiment and of the simulations. The load values of the three comparison points is shown in figure (5.10) with three orizontal black lines.

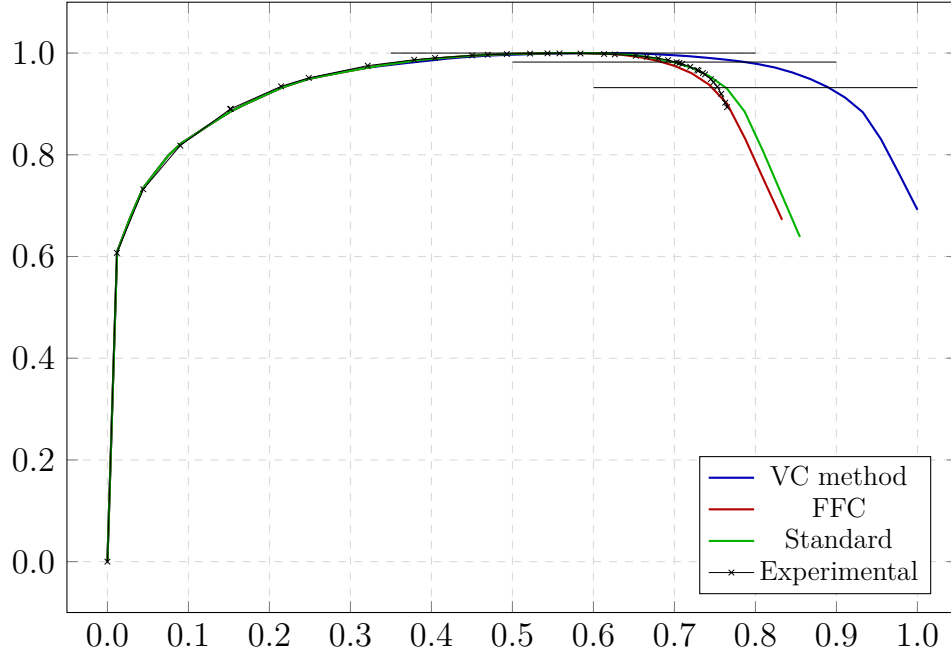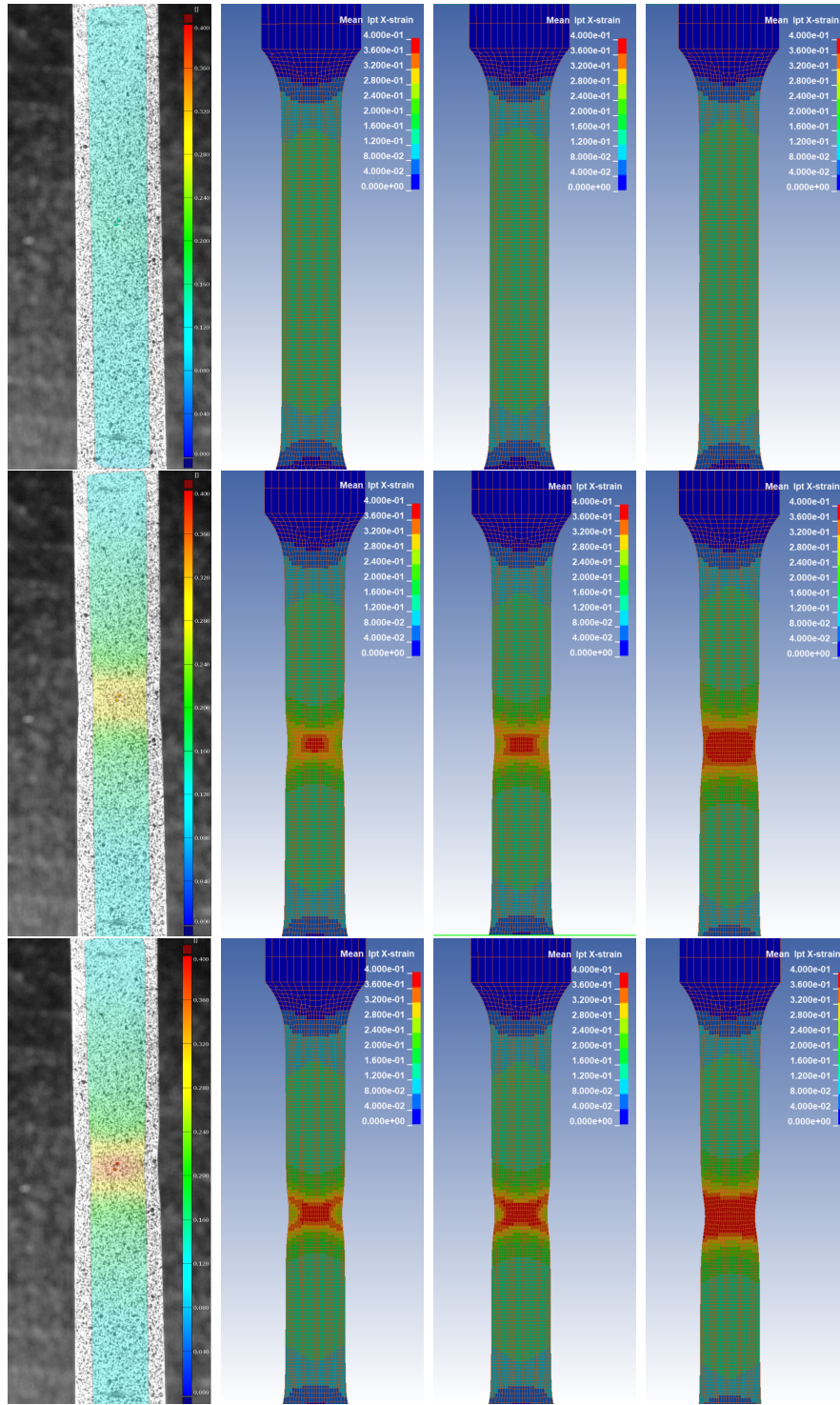Figure 5.10: DP800 engineering curve comparison

The same strain field comparison was carried and the four different fields are presented below in figure (5.11). The images, like in Section (5.4), show that the simulations over-estimate the strain. The implementation of a failure model can improve the results.

(a) DIC   (b) FFC   (c) Traditional   (d) VC

Figure 5.11: Strain field comparison

Table (5.2) shows the maximum measured strains at the load levels of the Figure (5.11):

Comparison load	DIC	FFC	Standard	VC
Max. Load	0.14	0.14	0.14	0.15
(Max. Load)·0.98	0.32	0.40	0.44	0.47
(Max. Load)·0.93	0.37	0.52	0.57	0.64

Table 5.2: Maximum measured true strain along the specimens length

5.6   Result discussion

It is possible to recognize some similarities in the results from both materials: the two optimized yield curves are better at portraying the localization of strains, particularly in the more brittle MS1500 where the "VC" method fails. In that case, the "VC" curve presents accurate results until the point of uniform elongation but after that it struggles to generate in the model the proper strain distribution and provides a material that is incredibly ductile. The higher computational cost of running an optimization is offset by a more accurate prediction of the material behavior. The results from the DP800 are more uniform, with also the "VC" model presenting accurate results in the strain field evolution, but the two optimized curves are both more accurate in terms of results. These findings lead to believe that the "VC" method is more suited for ductile materials, while the other two can adapt to both ductile and brittle materials, with better accuracy in both cases. Further studies are needed to consolidate this result.

Comparing the two optimization techniques for both the materials the optimizations reached the solution in less iterations for the Full field calibration

method. The table (5.3) shows the actual numbers.

| Optimization	Iterations	total simulations
MS1500 FFC	8	41
MS1500 Standard	12	61
DP800 FFC	11	56
DP800 Standard	13	66

Table 5.3: Simulations per optimization

The two optimization techniques produced comparable results, but the strain field resulting from the "FFC" curve resembles more closely the one measured on the experimental sample. Concerning the MS1500 specimen the experimental sample experienced the failure on one of its sides not in the middle, but to maintain symmetry in the simulations the strains measured in the failure region were mapped on the center of the *big* specimen as shown in the figure (5.4). The strain fields present a small delay in the initiation of the localization of strains that is present across the models, and especially marked in the "VC" model.

One interesting observation regarding all the results is that the yield locus in the simulations of both materials is characterized by the same approximate "X" shape. The shape of the localization depends on the yield curve and on the element size[17] indicating that, because all the simulations were run on the same mesh, the chosen plasticity model "Hockett & Sherby" could have a big influence in the correct strain field simulation. For the MS1500 which presented a slip plane the shape of the yield locus was favorable to the optimization, while for the DP800 which showed a more typical necking the strain fields resulting from the "Hockett & Sherby" model were not as good

as in the other material and more uniform across all the models.

Below in the Figure (5.12) are presented the metamodels that describe the influence of C and n on the optimization score calculated by LS-OPT for the MS1500.
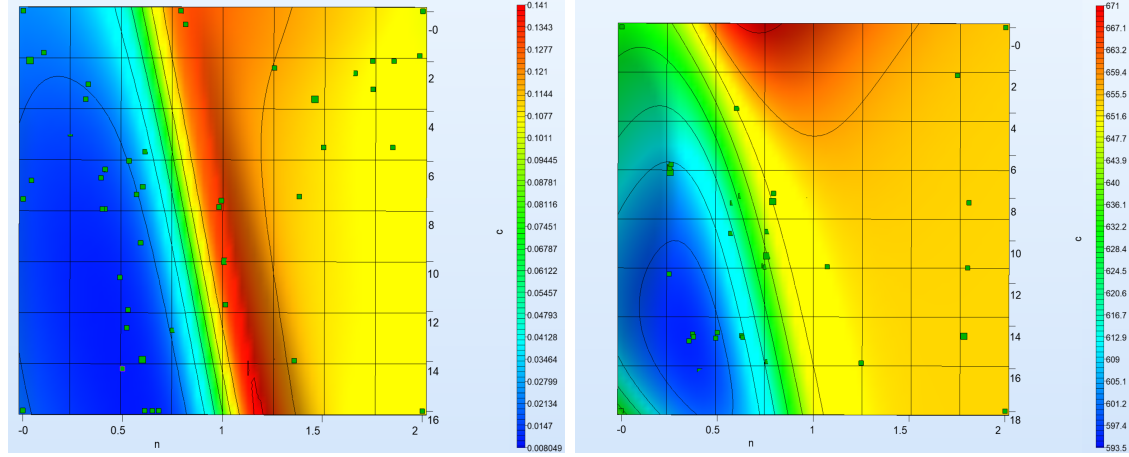
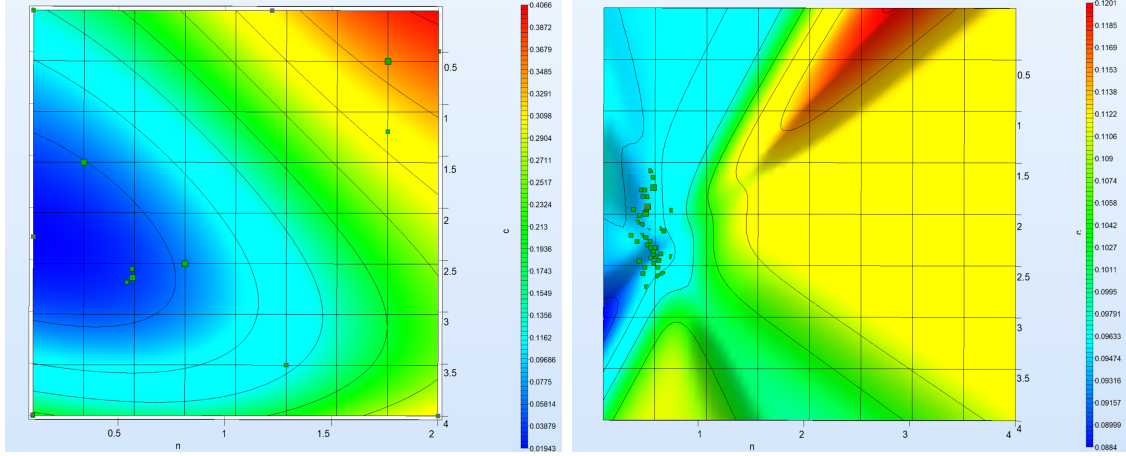(a) Standard   (b) FFC

Figure 5.12: Metamodel comparison

The scales on the images represent the score that the optimization algorithm assigns to the simulation points. It is different in the two images because for the "Standard" optimization the matching algorithm has to compare only one curve with the experimental one, while for the "FFC" analysis the algorithm compares several curves and sums up the scores for each of them. The range of scores can be used to compare two different combination of values only inside the same optimization, not across different ones. The two metamodels appear quite similar in overall shape, with the "FFC" one having the area around the optimum more localized, the score rises more significantly in its neighbourhood.

The Figure (5.13) shows the metamodels of the DP800 optimization: The

(a) Standard   (b) FFC

Figure 5.13: Metamodel comparison

same conclusions apply to the DP800 metamodels, but the difference between the two is more evident here. This difference can be explained in the nature of the two materials subject of the study: the DP800 being a much more ductile material presents a more pronounced plasticity region. It reached 18% elongation, while the MS1500 around 4-5% leaving less to the optimization to result in a difference between the metamodel. The parameters searched for in the optimization are determined based on the plastic behavior of the material. The engineering curve represents an attempt at characterizing the physics happening inside the material and it could be non significant for the actual behavior of the material. This is apparent when comparing the strain fields of both materials, even with very similar engineering stress-strain curves. The Tables (5.1) and (5.2) together with the corresponding images (Figures (5.7) and (5.9)) show how "FFC" performed better in the characterization of the material, thanks to its different objective.

Chapter 6

Failure optimization

Summary

This chapter follows the structure of Chapter (5) and describes the optimization problem formulation for the determination of the GISSMO parameters. For this part only the MS1500 steel is considered since for the DP800 the necessary specimen geometries to be tested were not available. To characterize GISSMO, 28 parameters are defined and they are the free parameters for the two optimizations. One is prepared the standard way and the other using the full field calibration method. The optimization results are then compared to the experimental data.

6.1   Input file preparation

The preparation of the GISSMO damage model is focused on finding the right values for the damage exponent n, the fading exponent m and the two curves function of the triaxiality that modulate the accumulation of the damage and of the instability: $\epsilon_f(\eta)$ and $\epsilon_{crit}(\eta)$. As described in Chapter (4) n and $\epsilon_f(\eta)$ regulate the damage accumulation, while m and $\epsilon_{crit}(\eta)$ regulate the accumulation of the instability parameter. It was first attempted to prepare the optimizations discretizing the two plastic strain curves with 5 points in correspondence of the triaxiality values expected by the test specimen geometry. The theoretical triaxiality values for the 5 geometries is shown in the table (6.1):

This approach intended to use each experimental test to tune the failure

Specimen	Triaxiality
Big	0.33
mini	0.33
notched	0.45
doublenotched	0.55
shear 45	0.25

Table 6.1: Theoretical triaxiality values

at the corresponding theoretical triaxiality value. In reality the triaxiality that is present in the simulation each geometry does not coincide with the theoretical value. It changes with time and depending on the location of the node it can be higher or lower than expected. The results that yielded from this approach were not satisfactory. The variability of the triaxiality in the simulations was too high to be properly portrayed with a curve parametrized with 5 values. To improve the match new optimizations were implemented

using 13 parameters for each curve together with the 2 for the exponents, adding up to 28 parameters per optimization. The points selected to discretize the curve are highlighted in the figure (6.1) with vertical lines. The figure (6.1) also shows the typical curves of a steel material and in particular the failure strain presents:

- high resistance for negative triaxiality

- lower resistance for shear cases (triaxiality between 0 and 0.25/0.3)

- higher for cases of uni-axial tension

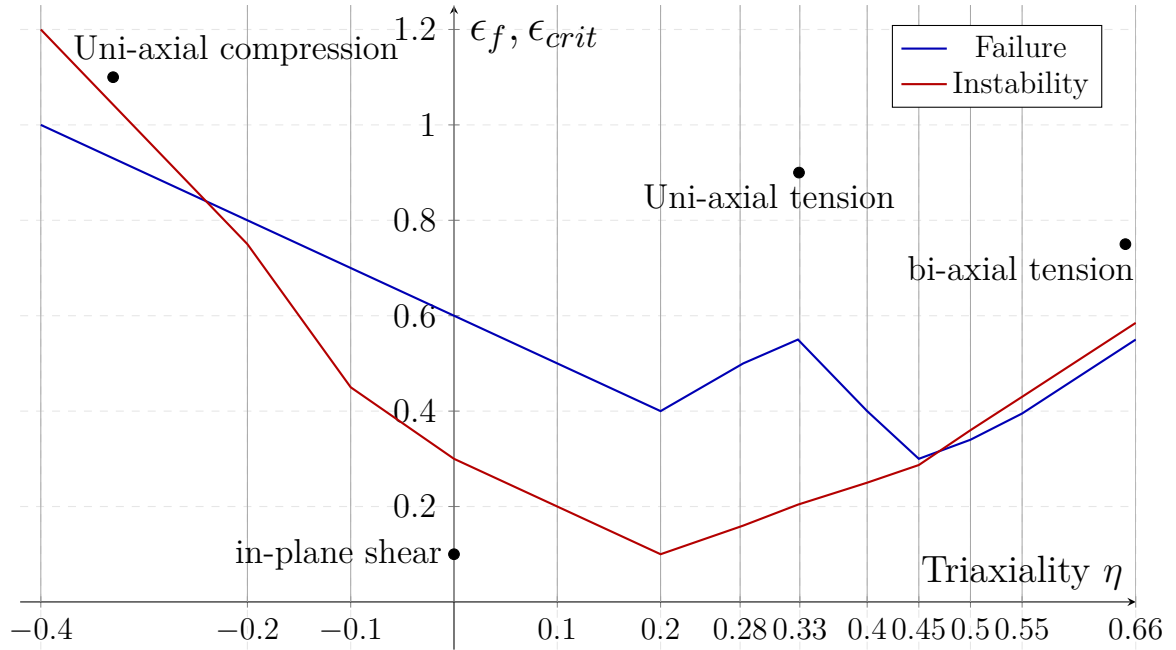- is lower again, to then rise for cases of bi-axial tension

Figure 6.1: GISSMO model objective curves

The instability curve was initially modelled to the shape of a parabola,

shown in red in figure (6.1), following the indications of DYNAmore GmbH laboratory's technicians. The curves shown in figure (6.1) represent the starting guess for the optimizations, and will differ from the final result.

6.2 LS-OPT optimizations

After the selection of the free parameters for the optimizations the LS-OPT projects were prepared, they are presented below in figure (6.2).
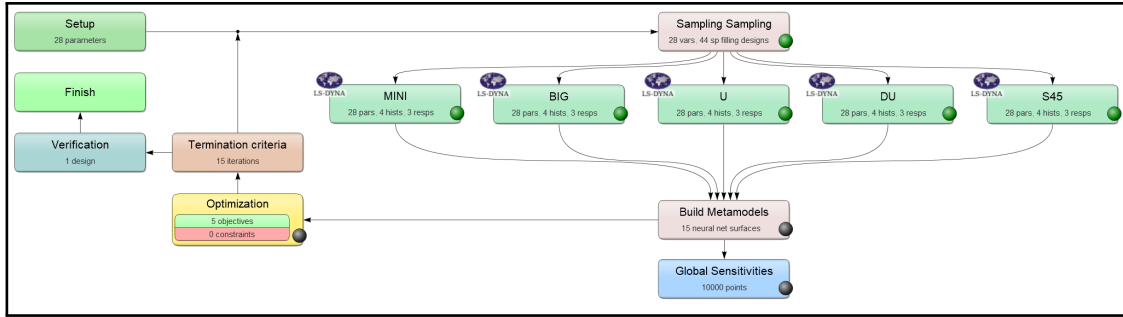

Figure 6.2: LS-OPT GISSMO optimization

The two new optimizations share almost the same structure with the yield curve optimizations, with the difference that now five stages are present and the optimization objective takes into account five contribution, coming from each one of the stages. 44 simulations per stage must be performed every iteration. The selected optimization strategy was the same: FFNN and sequential optimization. The next two sections discuss the differences between the two new optimizations: GISSMO standard and FFC.

6.2.1 Standard optimization

The optimization objective is the sum of the five different specimens objectives, each of them is the score that evaluates the match between the

simulation's force-engineering strain and the experimental one. The same procedure described in section (5.2.1) is applied to the five stages.

6.2.2 Full Field calibration optimization

Like explained in the previous section, the GISSMO optimization was prepared likewise. The procedure is described in section (5.2.2) and was performed for the five different geometries.

6.3 Result discussion

It was not possible to conclude the "FFC" optimization prepared for the GISSMO model. The following discussion describes the results from the standard optimization, showing in where it was effective and what was concluded. Figure (6.3) shows the starting $\epsilon_f(\eta)$ and $\epsilon_{crit}(\eta)$ curves together with the one resulted from the optimization:
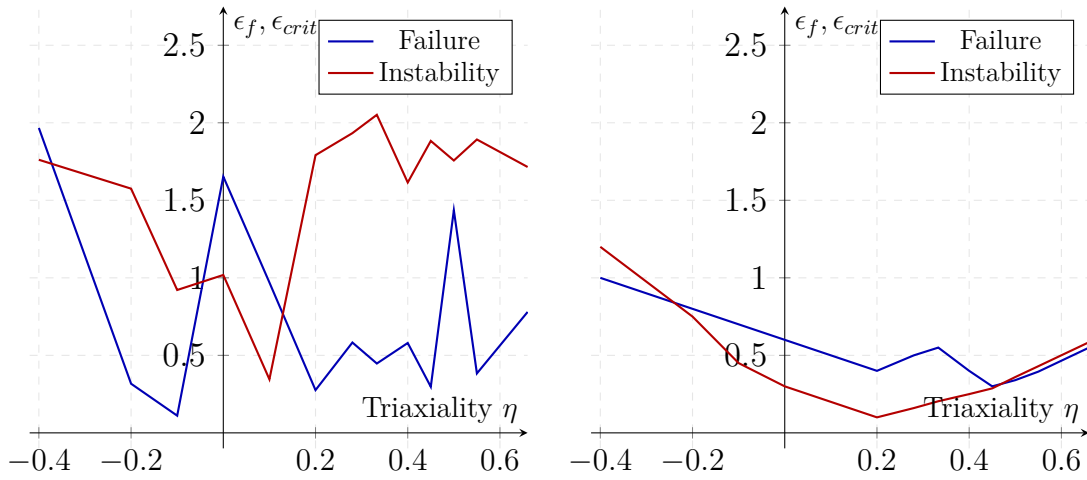

Figure 6.3: GISSMO model original and final objective curves

Below in figure (6.4), (6.5), (6.6) and (6.7) are presented the normalized force-engineering strain curves of the four geometries analyzed in the optimization that resulted from the optimal simulation, which used the curves in figure (6.3), $n = 1.14$ and $m = 0.195$:
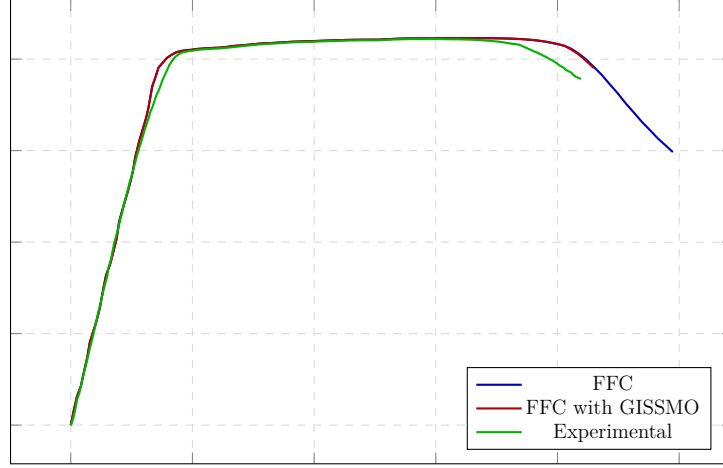

Figure 6.4: GISSMO damage model effect on the *big* sample
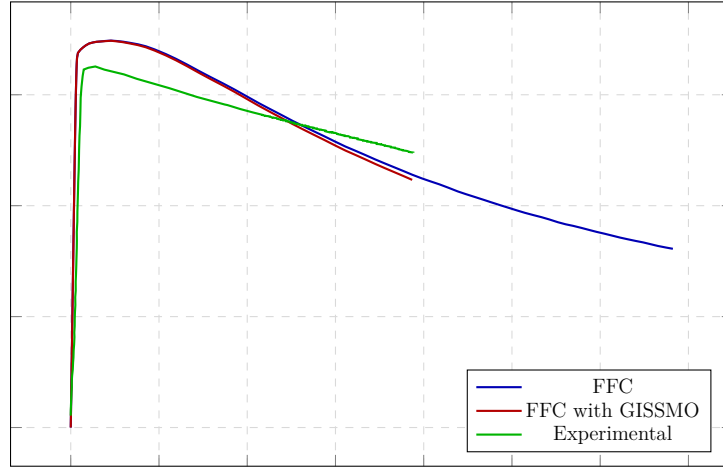

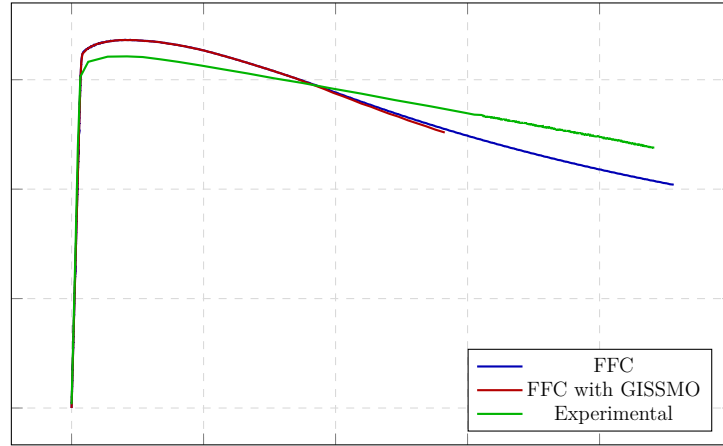Figure 6.5: GISSMO damage model effect on the *Doublenotched* sample

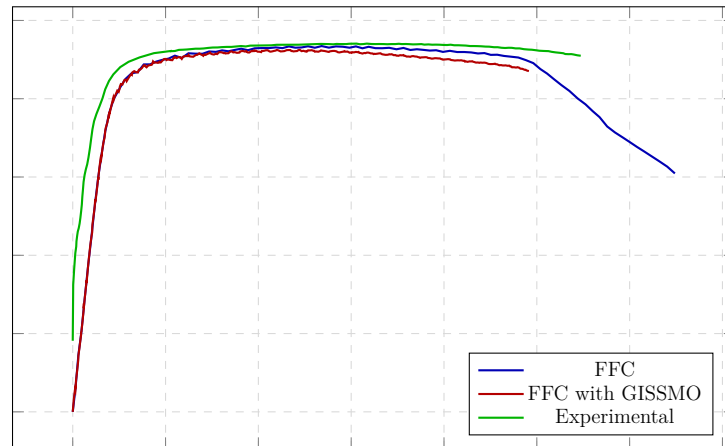Figure 6.6: GISSMO damage model effect on the *Notched* sample

Figure 6.7: GISSMO damage model effect on the *Shear* 45° sample

The graphs illustrate how the GISSMO model is able to more closely reproduce the material failure. Not all geometries are simulated with the same level of accuracy. It is possible to assume that most of the discrepancies are dependent on the material model chosen for the simulation: it is isotropic and it can not properly portray the MS1500, which showed an orthotropic

85

behavior in some samples.

The GISSMO damage model is also able to reduce the maximum strain measured inside the material, making the overestimation of the strain field that was presented in the previous chapter less present across all the models. After the characterization of the parameters that provide the needed GISSMO model is necessary to perform the regularization of the damage model, to make it applicable in more complex simulations. GISSMO presents a curve that is able to scale the damage effects as a function of the mesh size, in particular for shell elements the critical length is the shortest side. The regularization is a trivial process that requires to iteratively modify the regularization curve until the results are no longer mesh dependent. It is outside the scope of this work and it is not included in this dissertation.

Chapter 7

Conclusions

In this work a framework of experiments and simulations was built to evaluate the effectiveness of the "Full field calibration" method applied to material parameters identification. Inside the typical work flow to characterize a material the "FFC" method has been compared to other two for the determination of the yield curve and with just one in the GISSMO damage model characterization. The results of the first part of the analysis concerning the yield curve point out to the poor quality of results that are obtained from the "VC" method, while highlight how both the "FFC" and "Standard" can perform quite accurately for both brittle and ductile materials. The "FFC" method presents a slight advantage when comparing the actual strain path of the specimens and the maximum measured strain values. A possible future study could furthermore assess how much they differ in terms of accuracy for more materials.

The value of the "FFC" method for the determination of GISSMO parameters is still an open question and this work can be of help in the formulation of new means to improve the characterization of materials.

Bibliography

[1] Bridgman P.W., *The Effect of Hydrostatic Pressure on the Fracture of Brittle Substances*, Journal of Applied Physics, Vol. 18, p. 246, 1947.

[2] https://commons.wikimedia.org/wiki/File:Stress_in_a_continuum.svg

[3] Huber M.T., *Czasopismo Techniczne*, Lemberg, Austria, Vol. 22, 1904.

[4] Von Mises R., *Mechanik der Festen Korper im Plastisch Deformablen Zustand*, Nachr. Ges. Wiss. Gottingen, 1913.

[5] Khan S. K., Huang S., *Continuum Theory of Plasticity*, Chap. 4, USA, 1995.

[6] https://commons.wikimedia.org/wiki/File:Axial_stress_noavg.svg

[7] https://commons.wikimedia.org/wiki/File:Yield_surfaces.svg

[8] https://www.nde-ed.org/TermsConditions/termsconditions.htm

[9] Hockett J.E., Sherby O.D., *Large Strain deformation of polycrystalline metals at low homologous temperatures*, Journal of the Mechanics and Physics of Solids 23, pp. 87-98, 1975.

[10] Brünig M. et al., *A ductile damage criterion at vaious stress triaxialities*, Int. J. Plasticity, pp. 1731-1755, 2008.

[11] Lemaitre J., *A Continuous Damage Mechanics Model for Ductile Fracture*, J. Mat. Tech., 107, pp. 83-89, 1985.

[12] *LS-OPT user manual*

[13] Ilg C. et al., *Application of a Full-Field Calibration Concept for Parameter Identification of HS-Steel with LS-OPT*, 15th Int. LS-Dyna user conference.

[14] Lionello G., Cristofolini L., *A practical approach to optimizing the preparation of speckle patterns for digital-image correlation*, Measurement Science and Technology, Volume 25.

[15] F. Andrade et al., *On the Prediction of Material Failure in LS-DYNA®: A Comparison Between GISSMO and DIEM*, 13th Int. LS-Dyna user conference.

[16] *LS-DYNA user manual*

[17] G. A.Henshall et al., *Unified Constitutive Laws of Plastic Deformation*, Pages 153-227, 1995